

# Leading-edge-vortex tailoring on unsteady airfoils using an inverse aerodynamic approach

Cite as: Phys. Fluids **34**, 057107 (2022); <https://doi.org/10.1063/5.0090328>

Submitted: 05 March 2022 • Accepted: 21 April 2022 • Published Online: 11 May 2022

 Arun Vishnu Suresh Babu,  Shreyas Narsipur, Matthew Bryant, et al.

## COLLECTIONS

 This paper was selected as Featured



[View Online](#)



[Export Citation](#)



[CrossMark](#)

## ARTICLES YOU MAY BE INTERESTED IN

[Effects of wing-body interaction on hawk moth aerodynamics and energetics at various flight velocities](#)

[Physics of Fluids](#) **34**, 051915 (2022); <https://doi.org/10.1063/5.0087161>

[Aerodynamic characteristics of flexible flapping wings depending on aspect ratio and slack angle](#)

[Physics of Fluids](#) **34**, 051911 (2022); <https://doi.org/10.1063/5.0094820>

[Swimming of an inertial squirmer array in a Newtonian fluid](#)

[Physics of Fluids](#) **34**, 053303 (2022); <https://doi.org/10.1063/5.0090898>

[LEARN MORE](#)

## APL Machine Learning

Open, quality research for the networking communities

MEET OUR NEW EDITOR-IN-CHIEF



# Leading-edge-vortex tailoring on unsteady airfoils using an inverse aerodynamic approach

Cite as: Phys. Fluids 34, 057107 (2022); doi: 10.1063/5.0090328

Submitted: 5 March 2022 · Accepted: 21 April 2022 ·

Published Online: 11 May 2022



View Online



Export Citation



CrossMark

Arun Vishnu Suresh Babu,<sup>1,a)</sup>  Shreyas Narsipur,<sup>2</sup>  Matthew Bryant,<sup>3</sup> and Ashok Copalarathnam<sup>3</sup> 

## AFFILIATIONS

<sup>1</sup>Department of Mechanical Engineering and Engineering Science, University of North Carolina at Charlotte, Charlotte, North Carolina 28223, USA

<sup>2</sup>Department of Aerospace Engineering, Mississippi State University, Mississippi State, Mississippi 39762, USA

<sup>3</sup>Department of Mechanical and Aerospace Engineering, North Carolina State University, Raleigh, North Carolina 27695, USA

<sup>a)</sup>Author to whom correspondence should be addressed: [asures10@uncc.edu](mailto:asures10@uncc.edu)

## ABSTRACT

In this paper, we present an approach to obtain a desired leading-edge vortex (LEV) shedding pattern from unsteady airfoils through the execution of suitable motion kinematics. Previous research revealed that LEV shedding is associated with the leading-edge suction parameter (LESP) exceeding a maximum threshold. A low-order method called LESP-modulated discrete vortex method (LDVM) was also developed to predict the onset and termination of LEV shedding from an airfoil undergoing prescribed motion kinematics. In the current work, we present an inverse-aerodynamic formulation based on the LDVM to generate the appropriate motion kinematics to achieve a prescribed LESP variation, and thus, the desired LEV shedding characteristics from the airfoil. The algorithm identifies the kinematic state of the airfoil required to attain the target LESP value through an iterative procedure performed inside the LDVM simulation at each time step. Several case studies are presented to demonstrate design scenarios such as tailoring the duration and intensity of LEV shedding, inducing LEV shedding from the chosen surface of the airfoil, promoting or suppressing LEV shedding during an unsteady motion on demand, and achieving similar LEV shedding patterns using different maneuvers. The kinematic profiles generated by the low-order formulation are also simulated using a high-fidelity unsteady Reynolds-averaged Navier-Stokes method to confirm the accuracy of the low-order model.

Published under an exclusive license by AIP Publishing. <https://doi.org/10.1063/5.0090328>

## I. INTRODUCTION

Leading-edge vortex (LEV) shedding is a characteristic flow feature in many airfoil and wing unsteady flows, often contributing significantly to the forces and moments<sup>1</sup> and causing dynamic stall.<sup>2</sup> Unsteady flows dominated by LEV formation are observed in nature on swimming and flying animals and seeds,<sup>3–5</sup> where the LEV helps achieve higher lift. In engineering, while there is usually an emphasis on avoiding LEV formation such as on rotorcraft,<sup>6,7</sup> wind turbines,<sup>8</sup> and micro-air vehicles,<sup>9</sup> there are also devices like flapping-wing energy harvesters<sup>9</sup> that are designed to harness the beneficial effects of LEVs on the forces and moments.<sup>9–11</sup> Because unsteady flows with attendant LEV formation are a result of motion kinematics<sup>12–18</sup> and/or gust encounters,<sup>19–22</sup> research efforts have explored the design of suitable motion kinematics to achieve desired force or flow behaviors. Although various efforts have been made to combine pitch, heave, and surge motions to either achieve desired force histories,<sup>23,24</sup> to cancel gust effects,<sup>25</sup> or for gust generation using oscillating foils,<sup>26</sup> most of the analytical approaches suitable for designing a motion to achieve

desired flow/force behaviors work only for nominally attached-flow conditions where the motion and gust effects can be superposed. In situations where LEV effects are dominant, the flow nonlinearity precludes the use of linear superposition approaches. Rival *et al.*<sup>27</sup> conducted a detailed study of the effect of various kinematics on the LEV formation on unsteady airfoils and suggested the possibility of regulating the LEV characteristics by carefully tuning the airfoil motion. It may be argued that tailoring the LEV characteristics by designing appropriate motion kinematics may be a good first step toward regulating force and moment behaviors in LEV-dominated airfoil flows. In this work, we present an approach for tailoring the LEV formation by appropriate design of pitch/heave kinematics. This approach, which relies on a new inverse formulation of a low-order prediction method for unsteady airfoils that can handle intermittent LEV shedding, avoids the limitations of earlier approaches which were mostly confined to attached-flow situations.

The growth of interest in flapping wings along with the advancement of experimental techniques and computational capabilities in the

past few decades have facilitated a detailed understanding of the mechanisms and phenomena associated with dynamic stall and LEV formation.<sup>28–33</sup> Reynolds-averaged Navier–Stokes (RANS) computations are currently widely used by researchers to explore LEV formation and dynamics in unsteady airfoils and wings.<sup>32,34–36</sup> The RANS-based studies by Ramesh *et al.*<sup>37</sup> and Narsipur *et al.*<sup>38</sup> reveal the connection between the onset of LEV shedding and the criticality of the suction at the airfoil leading edge. Large-eddy simulation (LES) studies help to unravel the fine features in turbulent regimes such as leading-edge shear-layer instabilities<sup>39</sup> and the bursting of laminar separation bubbles<sup>40</sup> associated with LEV formation. Although expensive, direct-numerical simulations (DNS) provide invaluable information about the finest details of complex flows such as how a Kelvin–Helmholtz instability generated at the leading edge influences the formation and dynamics of the LEV.<sup>41</sup> Modern experimental surface and flowfield diagnostics techniques have helped to identify the role of various factors such as effective angle of attack,<sup>42</sup> forward movement of the trailing separation point,<sup>43</sup> external flow disturbances,<sup>44</sup> leading-edge shear-layer angle,<sup>45</sup> shear-layer curvature,<sup>46</sup> characteristic feeding shear-layer velocity,<sup>47</sup> leading-edge flow unsteadiness,<sup>48</sup> and secondary vortical structures<sup>45</sup> affecting the formation and evolution of the LEV. They have also helped quantify the spatial and temporal evolution of the LEV and its strength.<sup>8,27,47,49,50</sup>

Theoretical approaches to model and predict the flow phenomena on unsteady wings complement the experimental and computational studies. While some of the earlier works focused on predicting only the loads,<sup>51,52</sup> later works have attempted to model the flowfield features, in particular the formation and dynamics of the LEV and its contribution to the flowfield evolution and unsteady loads.<sup>37,53–57</sup> In previous research, Ramesh *et al.*<sup>37</sup> demonstrated that the onset and termination of LEV shedding from unsteady airfoils is connected with the criticality of the leading-edge suction parameter (LESP), which is a non-dimensional measure of the suction at the leading edge. A low-order method, called the LESP-modulated discrete vortex method (LDVM) was also developed by combining a large-angle unsteady thin airfoil theory with a discrete-vortex method to predict the LEV shedding patterns and the associated transient loads. LDVM was validated extensively for unsteady airfoils in uniform flow at low to moderate  $Re$  ( $Re \approx 10\,000$ – $100\,000$ ) by Ramesh *et al.*<sup>37</sup> using experimental and computational results. Some recent works have closely examined LESP, furthering the insight into the behavior and application in different scenarios such as various  $Re$  regimes, unsteady finite wings, and unsteady airfoils encountering external disturbances.<sup>38,43,44,58–60</sup> Recent analytical and numerical formulations have also helped gain an understanding of the effects of LEV and free vortices in the flow on the airfoil forces and leading-edge suction through the use of various

vortex maps<sup>44,61,62</sup> and force partitioning.<sup>63</sup> These contributions have resulted in greater insight into the flow physics of LEVs and their effects of airfoil forces.

In this work, we present an inverse-aerodynamic approach based on the LDVM to design pitch/heave motion kinematics to tailor the duration and severity of LEV shedding from an unsteady airfoil as well as to induce or suppress LEV shedding on-demand. The desired LEV shedding pattern is transcribed into a corresponding time-variation of the LESP, and the inverse approach is used to obtain the required motion kinematics that results in the given LESP variation and thus the desired LEV shedding pattern. The theory behind the LDVM method is outlined and the use of LES to predict LEV shedding from unsteady airfoils is demonstrated in Sec. II. The inverse-aerodynamic approach based on LDVM is formulated in Sec. III. A simplified approach based on quasi-steady thin-airfoil theory (QSTAT) is also presented. Several case studies are presented in Sec. IV to demonstrate the application of the inverse formulation to various scenarios. The predicted motion kinematics are simulated using an unsteady RANS computational fluid dynamics (CFD) method, and results are presented to validate the low-order results from the inverse-aerodynamic formulation. The predictions of the QSTAT-based approach are evaluated in Sec. V. Finally, the concluding remarks are presented in Sec. VI.

## II. BACKGROUND

We use the low-order two-dimensional unsteady aerodynamic model developed in previous research by Ramesh *et al.*<sup>37</sup> as the foundation for developing the current LEV-tailoring algorithm. This model combines a large angle unsteady thin airfoil theory with a discrete-vortex method to model the unsteady flowfield around airfoils undergoing arbitrary motion kinematics and compute the time-varying loads. The most important feature of this method is its capability to predict the initiation and termination of LEV shedding from airfoils with rounded leading edges for a wide range of operating conditions. This prediction is made based on a quantity called the leading-edge suction parameter (LESP) and hence is called LESP-modulated discrete-vortex method (LDVM). Below, we present the basic theoretical and numerical aspects of this method.

### A. The unsteady thin airfoil theory

Figure 1 shows an airfoil of chord  $c$  at time  $t$  undergoing arbitrary pitching and heaving kinematics while translating leftward with a speed  $U$ . The pitch and heave positions are denoted by the variables  $\theta$  and  $h$  in the inertial coordinate system  $Oxz$ . The variables  $\dot{\theta}$  and  $\dot{h}$  indicate the corresponding velocities.  $x_p$  represents the pivot point about which the airfoil executes the pitching motion. Also shown is a

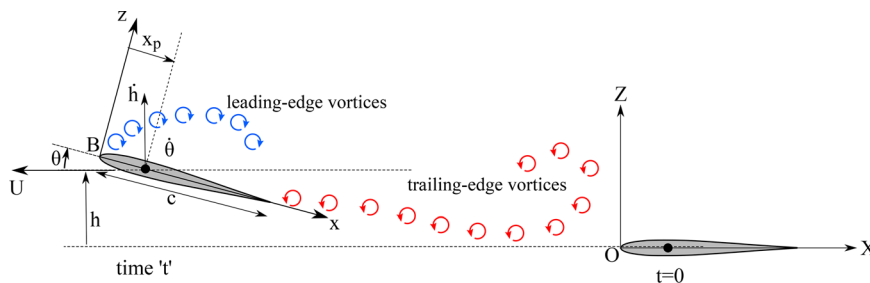


FIG. 1. A schematic showing the different variables used in the theoretical formulation.

body-fixed frame of reference  $Bxz$  with the origin at the leading edge, the  $x$  axis pointing in the chordwise direction, and the  $z$  axis pointing in the chord-normal direction. Both the frames coincide at  $t = 0$ .

Following the lines of thin-airfoil theory, the airfoil is represented by a continuous bound circulation distribution  $\gamma(x, t)$ . Using the Glauert transformation  $x = \frac{c}{2}(1 - \cos \nu)$ , we get

$$\gamma(\nu, t) = 2U_{ref} \left[ A_0(t) \frac{1 + \cos \nu}{\sin \nu} + \sum_{n=1}^{\infty} A_n(t) \sin(n\nu) \right], \quad (1)$$

where  $U_{ref}$  is an arbitrary reference velocity, typically set equal to  $U$ . The Fourier coefficients,  $A_n(t)$ , are to be obtained such that zero-normal-flow boundary condition is satisfied at every time instant  $t$ . This condition yields the following expressions for  $A_n$ :

$$A_0(t) = -\frac{1}{\pi} \int_0^{\pi} \frac{W(\nu, t)}{U_{ref}} d\nu, \quad (2)$$

$$A_n(t) = \frac{2}{\pi} \int_0^{\pi} \frac{W(\nu, t)}{U_{ref}} \cos(n\nu) d\nu, \quad n \geq 1. \quad (3)$$

Here,  $W$ , referred to as the downwash, is the velocity induced along the airfoil in the direction opposite to the normal to the camber line, and can be expressed as follows:

$$W(x, t) = \frac{\partial \eta}{\partial x} (U \cos \theta + \dot{h} \sin \theta + u_{ind}(x)) - U \sin \theta - \dot{\theta}(x - x_p) + \dot{h} \cos \theta - w_{ind}(x). \quad (4)$$

The term  $\frac{\partial \eta}{\partial x}$  represents the slope of the camber line. The terms  $u_{ind}(x)$  and  $w_{ind}(x)$  denote the velocity induced on the airfoil by all the free vortices in the flowfield in the  $x$  and  $z$  directions, respectively. The expression for downwash in Eq. (4) takes into account large pitch angle regimes at which the traditional small-angle approximations are not valid.

## B. The discrete vortex method

The vorticity shed from the airfoil is modeled using discrete vortices (DVs) released at every time step from the airfoil edges. Clockwise vorticity is considered positive. The components of velocity induced at a point  $(x, z)$  by a DV of strength  $\Gamma_k$  located at  $(x_k, z_k)$  are given by the Biot-Savart law with regularization using a vortex core,  $r_{core}$ , following the model proposed by Vatistas *et al.*<sup>64</sup>

$$(u, w) = \frac{\Gamma_k}{2\pi\sqrt{[(x_k - x)^2 + (z_k - z)^2]^2 + r_{core}^4}} (z - z_k, x_k - x), \quad (5)$$

where  $r_{core} = 0.02c$  is used following the implementation of Ramesh *et al.*<sup>37</sup> The vortices are convected using the local velocity induced at their locations due to all the other free vortices and the bound vorticity.

The prescribed motion of the airfoil and the resulting flowfield evolution are simulated in a series of discrete time steps. The flow chart in Fig. 2 shows the time-stepping procedure in the LDVM simulation.

### 1. TEV shedding

A discrete trailing-edge vortex (TEV) is shed from the airfoil at every time step in accordance with Kelvin condition. The TEV

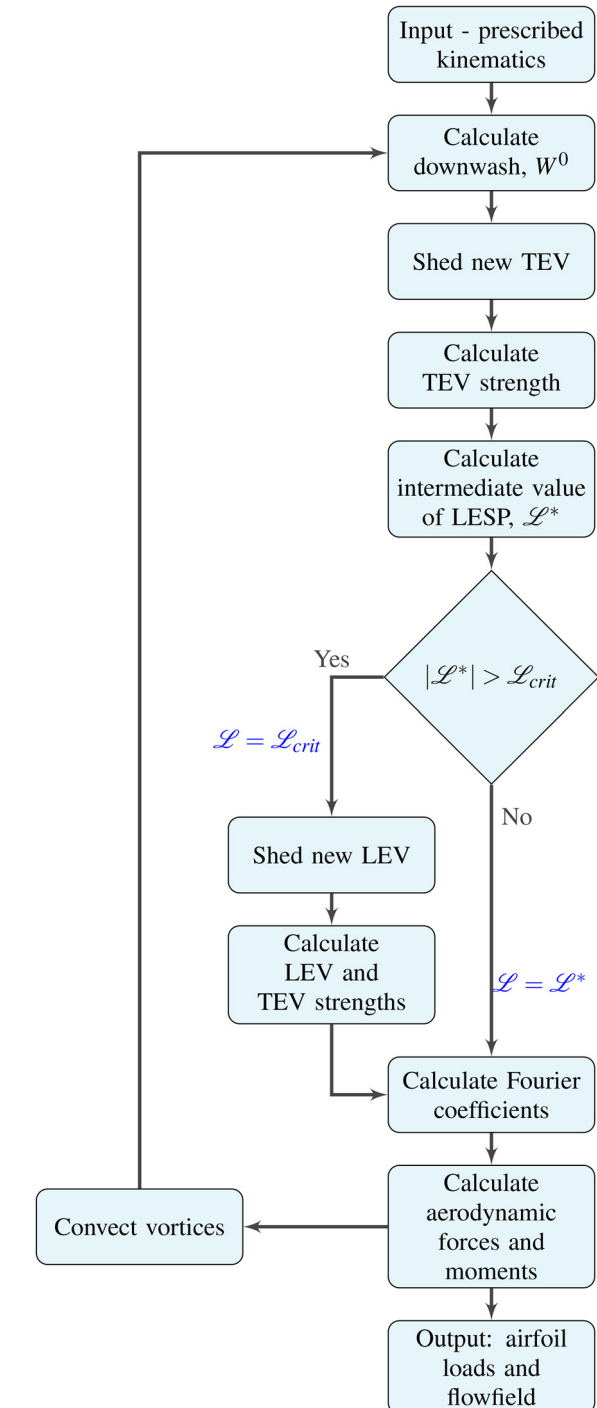


FIG. 2. Flowchart for the LDVM algorithm.

is placed at one-third of the distance between the trailing edge and the previously shed TEV. In the absence of LEV shedding, a discrete TEV of strength  $\Gamma_{TEV}^j$  is released at the  $j$ th time step such that

$$\Gamma_B^j + \Gamma_{TEV}^j = \Gamma_B^{j-1}, \quad (6)$$

where  $\Gamma_B = \int_0^\pi \gamma(\nu) d\nu = \pi c U_{ref} [A_0(t) + A_1(t)/2]$  is the bound circulation around the airfoil. The strength of the latest TEV can be obtained after some manipulation of Eq. (6) as

$$\Gamma_{TEV}^j = \frac{\Gamma_B^{j-1} + c \int_0^\pi W^0 (1 - \cos \nu) d\nu}{1 - c \int_0^\pi W'_{TEV} (1 - \cos \nu) d\nu}. \quad (7)$$

Here,  $W'_{TEV}$  is the downwash induced by a DV with unit-strength placed at the location of the latest TEV.  $W^0$  is the downwash due to all other factors excluding the latest TEV, obtained using Eq. (4).

## 2. LEV shedding

In previous research, Ramesh *et al.*<sup>37</sup> observed that flow separation and initiation of LEV formation occurs when the chordwise suction force at the leading edge exceeds a maximum threshold that can be supported by the leading-edge shape. A non-dimensional measure of this force, called the leading-edge suction parameter (LESP, denoted henceforth by  $\mathcal{L}$ ) is used to predict the onset and termination of LEV shedding. If the flowfield and the kinematic state of the airfoil are known at any given time instant,  $\mathcal{L}$  can be obtained using the resulting downwash as

$$\mathcal{L}(t) = -\frac{1}{\pi} \int_0^\pi \frac{W(x, t)}{U_{net}(t)} d\nu, \quad (8)$$

where  $U_{net}(t)$  is the time-dependent net-velocity magnitude due to the motion kinematics, including the forward speed and the instantaneous pitch and heave rates. As shown in greater detail in Narsipur *et al.*,<sup>38</sup> an appropriate  $U_{net}(t)$  is the magnitude of the vector sum of the forward speed, heave speed, and the velocity of the half-chord point due to the pitch rate, resulting in a  $U_{net}(t)/U$  is given by

$$\frac{U_{net}(t)}{U} = \sqrt{\left[ 1 + \frac{\dot{\theta}(t)c}{U} \left( \frac{1}{2} - \frac{x_p}{c} \right) \sin \theta(t) \right]^2 + \left[ \frac{\dot{h}(t)}{U} - \frac{\dot{\theta}(t)c}{U} \left( \frac{1}{2} - \frac{x_p}{c} \right) \cos \theta(t) \right]^2}. \quad (9)$$

It is often convenient to define the kinematics using convective time defined as  $t^* = tU/c$ . Then,  $U_{net}(t)/U$  can be rewritten in terms of non-dimensional pitch rate,  $\theta = \partial\theta/\partial t^* = \dot{\theta}c/U$ , and non-dimensional heave rate,  $h = \partial(h/c)/\partial t^* = \dot{h}/U$ , as

$$\frac{U_{net}(t)}{U} = \sqrt{\left[ 1 + \theta(t) \left( \frac{1}{2} - \frac{x_p}{c} \right) \sin \theta(t) \right]^2 + \left[ h(t) - \theta(t) \left( \frac{1}{2} - \frac{x_p}{c} \right) \cos \theta(t) \right]^2}. \quad (10)$$

In LDVM, LEV shedding is incorporated based on the hypothesis that  $\mathcal{L}$  cannot exceed a predetermined critical value,  $\mathcal{L}_{crit}$ . If, at any time step,  $\mathcal{L}$  tends to exceed  $\mathcal{L}_{crit}$ , a discrete LEV is released from the leading edge to ensure that  $\mathcal{L}$  is maintained at  $\mathcal{L}_{crit}$ .

At every time step, a discrete TEV is initially shed according to Eq. (7) assuming no LEV shedding. This gives a valid solution of the

flowfield that satisfies the Kelvin condition. This solution corresponds to an intermediate value of  $\mathcal{L}$ , denoted by  $\mathcal{L}^*$ . If the magnitude of  $\mathcal{L}^*$ ,  $|\mathcal{L}^*|$ , does not exceed  $\mathcal{L}_{crit}$ , the current solution without LEV shedding is acceptable. The intermediate values of the TEV strength and  $\mathcal{L}^*$  are set as the respective final values at the current time step and the simulation proceeds to the next time step. If  $|\mathcal{L}^*|$  exceeds  $\mathcal{L}_{crit}$ , the intermediate solution is not acceptable and LEV shedding needs to be accounted for. If  $\mathcal{L}^*$  is positive, then a clockwise DV is released, which automatically is convected to the upper surface, simulating LEV shedding from the upper surface. A negative  $\mathcal{L}^*$  will result in the shedding of a counterclockwise DV from the lower surface. A more acceptable solution is now obtained by simultaneously solving for the strengths of the latest LEV and the latest TEV so as to satisfy the Kelvin condition and to maintain  $\mathcal{L}$  at  $\mathcal{L}_{crit}$ . This problem can be formulated as a system of two linear equations where the unknowns are the strengths of the latest LEV and TEV:

$$[A] \begin{Bmatrix} \Gamma_{TEV} \\ \Gamma_{LEV} \end{Bmatrix} = \{B\}, \quad (11)$$

where

$$[A] = \begin{bmatrix} 1 - c \int_0^\pi W'_{TEV} (1 - \cos \nu) d\nu & 1 - c \int_0^\pi W'_{LEV} (1 - \cos \nu) d\nu \\ \int_0^\pi W'_{TEV} d\nu & \int_0^\pi W'_{LEV} d\nu \end{bmatrix} \quad (12)$$

and

$$\{B\} = \begin{Bmatrix} \Gamma_B^{j-1} + c \int_0^\pi W^0 (1 - \cos \nu) d\nu \\ -\pi U_{net} \mathcal{L}_{crit} - \int_0^\pi W^0 d\nu \end{Bmatrix}, \quad (13)$$

and  $W'_{LEV}(x)$  is the downwash due to a unit-strength DV placed at the location of the latest LEV. From the above discussion, it can be deduced that

$$\mathcal{L} = \begin{cases} \mathcal{L}^*, & \text{if } |\mathcal{L}^*| < \mathcal{L}_{crit}, \\ \mathcal{L}_{crit}, & \text{otherwise.} \end{cases} \quad (14)$$

The value of  $\mathcal{L}_{crit}$  for a given airfoil at a given Reynolds number can be predetermined using experimental or CFD data. This parameter has been observed to be largely independent of motion kinematics and hence can be used to predict the LEV shedding characteristics of the given airfoil at the given Reynolds number for a range of arbitrary motion kinematics.

## C. The unsteady loads

Once the solution of the flowfield at a given time step is known, the normal force per unit span can be obtained as

$$\begin{aligned} F_N = & \rho \pi c U_{ref} (U \cos \theta + \dot{h} \sin \theta) \left( A_0(t) + \frac{1}{2} A_1(t) \right) \\ & + \rho \pi c^2 U_{ref} \left( \frac{3}{4} \dot{A}_0(t) + \frac{1}{4} \dot{A}_1(t) + \frac{1}{8} \dot{A}_2(t) \right) \\ & + \rho \int_0^c u_{ind}(x) \gamma(x, t) dx + \rho c \dot{\Gamma}_{lev}, \end{aligned} \quad (15)$$

where  $\dot{\Gamma}_{lev}$  is the rate of vorticity shedding from the leading edge. The suction force per unit span of the airfoil is given by

$$F_s = \rho \pi c U_{ref}^2 A_0^2. \quad (16)$$

The normal-force coefficient  $C_n$  and the suction-force coefficient  $C_s$  can be obtained by non-dimensionalizing using the quantity  $\frac{1}{2} \rho U_{ref}^2 c$ . Then, the lift and drag coefficients are given by

$$C_l = C_n \cos \theta + C_s \sin \theta, \quad (17)$$

$$C_d = C_n \sin \theta - C_s \cos \theta. \quad (18)$$

The moment per unit span about an arbitrary reference point  $x_{ref}$  on the airfoil can be obtained as

$$M = x_{ref} F_N - \rho \pi c^2 U \left[ (U \cos \theta + h \sin \theta) \left( \frac{1}{4} A_0(t) + \frac{1}{4} A_1(t) - \frac{1}{8} A_2(t) \right) + c \left( \frac{7}{16} \dot{A}_0(t) + \frac{11}{64} \dot{A}_1(t) + \frac{1}{16} \dot{A}_2(t) - \frac{1}{64} \dot{A}_3(t) \right) \right] - \rho \int_0^c \left( \left( \frac{\partial \phi_{lev}}{\partial x} \right) + \left( \frac{\partial \phi_{tev}}{\partial x} \right) \right) \gamma(x, t) x dx - \rho \frac{c^2 \dot{\Gamma}_{lev}}{2}. \quad (19)$$

#### D. Validation of the LDVM

The LDVM has been validated extensively against high-fidelity CFD and experimental results for various cases involving different geometries, Reynolds numbers and motion kinematics.<sup>37,38,44,58</sup> Here,

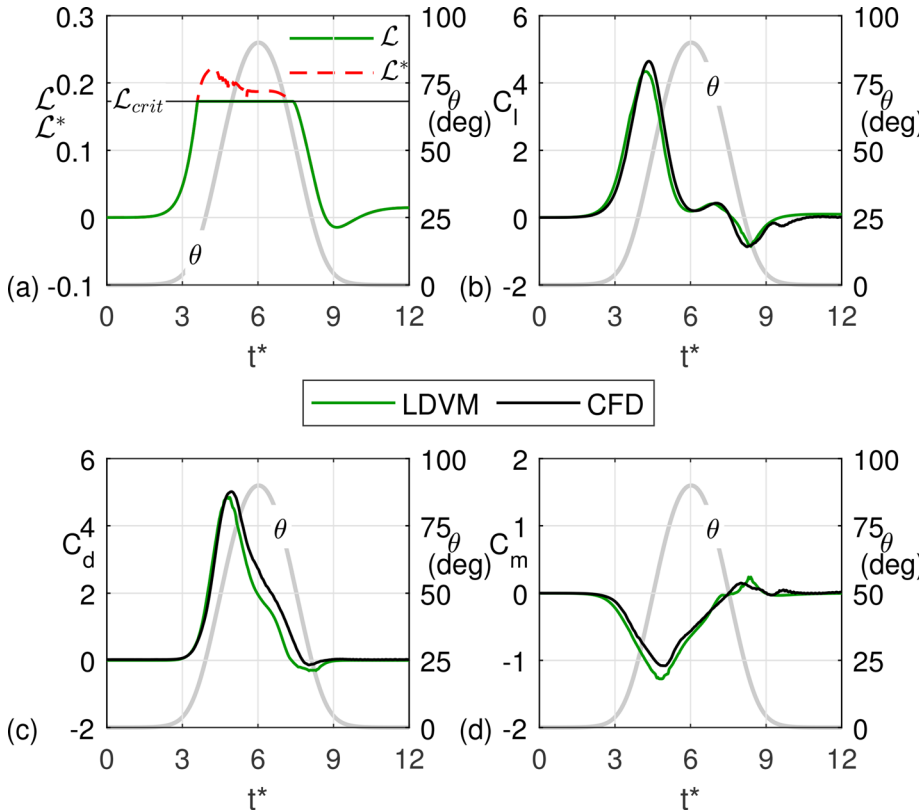


FIG. 3. Time variations of (a)  $\mathcal{L}$ , (b)  $C_l$ , (c)  $C_d$ , and (d)  $C_m$  for the validation case.

we present a validation of LDVM against unsteady Reynolds-Averaged Navier-Stokes (uRANS) results of a NACA0012 airfoil pivoted at the quarter-chord and undergoing a prescribed  $0^\circ$ – $90^\circ$ – $0^\circ$  pitch-up–return motion at a non-dimensional pitch rate,  $K = \dot{\theta}_c / 2 U_{ref}$ , of 0.4 at  $Re = 30\,000$ . The value of  $\mathcal{L}_{crit}$  for this airfoil- $Re$  combination is set as 0.17 based on results from Narsipur *et al.*<sup>38</sup>

The results of the validation study is shown in Fig. 3. Figure 3(a) shows  $\mathcal{L}$  increasing toward the positive critical value as the airfoil starts pitching up. During this phase of motion before the LEV initiation,  $\mathcal{L}$  and  $\mathcal{L}^*$  overlap. LEV initiation occurs at  $t^* = 3.6$  when  $\mathcal{L}^*$  exceeds the critical value of  $\mathcal{L}_{crit} = 0.17$ . The co-plotted  $\mathcal{L}^*$  value continues to be greater than  $\mathcal{L}_{crit}$  until  $t^* = 7.4$ , indicating uninterrupted LEV shedding during this time period. Discrete LEVs are shed from the leading edge during this time interval, and their strengths are determined to maintain  $\mathcal{L}$  at  $\mathcal{L}_{crit}$ . LEV shedding terminates when  $\mathcal{L}^*$  falls below the critical value. After this event,  $\mathcal{L}$  and  $\mathcal{L}^*$  overlap once again.

Observations of Figs. 3(b)–3(d) show that the lift, drag, and moment coefficient predictions by the LDVM compare very well with CFD data with a slight underprediction in  $C_d$  during the shedding process and in peak  $C_l$  and  $C_m$  by the LDVM. To further explore the details of LDVM and discussions on the accuracy of its predictions, refer to the previous works on LDVM.<sup>37,44,65,66</sup>

Figure 4 overlays the leading- and trailing-edge vortex flow pattern predictions from the LDVM on top of the vorticity contours from the CFD solutions at six time instants from just after LEV initiation to slightly after the LEV convects past the trailing edge. Results show the

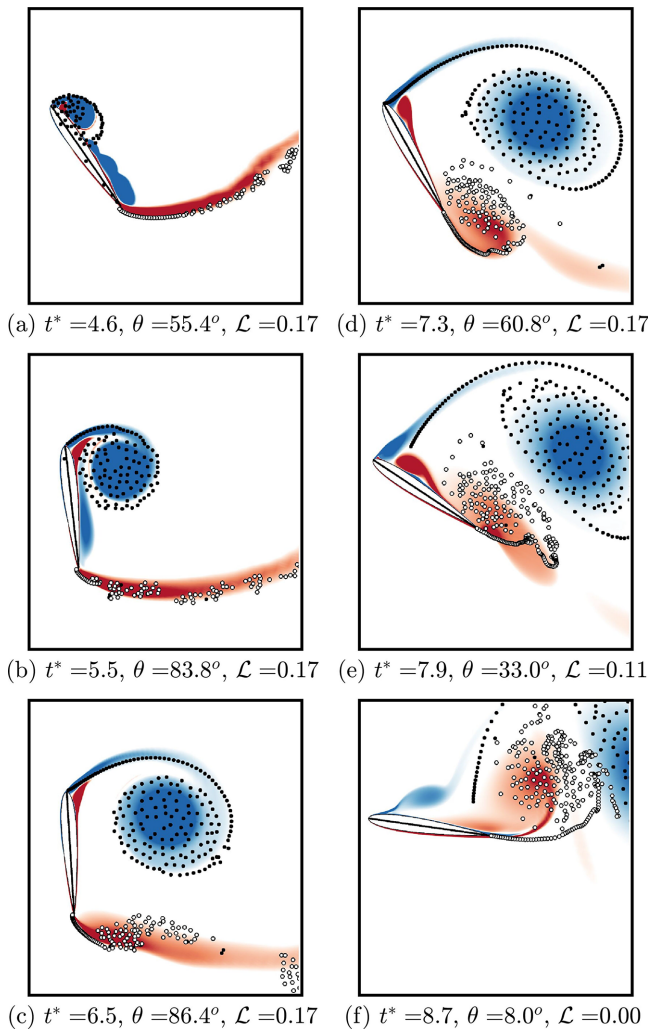


**FIG. 4.** Flow visualization for the validation case. The respective time instants are shown in panels (a)–(f). Color contours are vorticity contours from CFD. Markers are DVs from LDVM: filled markers are LEVs and open markers are TEVs.

LDVM-predicted LEV flow patterns compare excellently with CFD data while the TEV flow patterns show small discrepancies for  $t^* > 7.3$ .

### III. METHODOLOGY: THE INVERSE-AERODYNAMIC FORMULATION FOR LEV TAILORING

Here, we present a strategy to tailor the features of an LEV shed from an unsteady airfoil through the execution of a suitable kinematic profile. This method can be employed, for instance, to start and stop LEV shedding from an airfoil at prescribed instants of time, to induce LEV shedding from the upper or lower surface of the airfoil on demand, and to tailor the strength of an LEV shed during an unsteady motion. In LDVM, the initiation and termination as well as the intensity of LEV shedding is determined by the intermediate value of LESP,  $\mathcal{L}^*$ , at every time step. Thus, these aspects of LEV shedding can be customized by achieving an appropriate  $\mathcal{L}^*$  variation. In other words, the problem translates to designing a suitable maneuver that will

generate a given  $\mathcal{L}^*$  variation. Below, we first formulate a “full” inverse-aerodynamic approach based on LDVM to identify a motion kinematics that will result in a prescribed  $\mathcal{L}^*$  variation and thus in a desired LEV shedding pattern from an unsteady airfoil. This full inverse approach uses the LDVM code, which takes into consideration the effects of the DVs in the flowfield, for the inverse solution. We also present a simplified inverse approach using quasi-steady thin airfoil theory (QSTAT), which does not take the effects of the DVs into consideration, and is therefore approximate. The advantage of the simplified QSTAT is that it solves a simple expression, does not require the LDVM formulation and code, and provides insight. The result of the simplification, however, is that it leads to inaccurate results when used in situations dominated by vortex shedding, as shown in Sec. IV.

#### A. Full inverse formulation using LDVM

The idea behind the inverse formulation is that once a flow solution is obtained at time step  $j$ , a commanded value of  $\mathcal{L}^*$ , denoted by  $\mathcal{L}_c^*$ , can be achieved at the next time step,  $(j+1)$ , by solving for the kinematic state of the airfoil  $[\theta \ h \ \dot{\theta} \ \dot{h}]_{(j+1)}^T$  for  $(j+1)$  that satisfies the following nonlinear equation:

$$[\mathcal{L}_c^* - \mathcal{L}^*]_{(j+1)} = 0, \quad (20)$$

where,  $\mathcal{L}^*$ , given by Eq. (8), depends on the chordwise distribution of downwash,  $W(x, t)$ , at time  $j+1$ , which in turn depends on the values of the state variables  $[\theta \ h \ \dot{\theta} \ \dot{h}]^T$  at time  $(j+1)$ , as given by Eq. (4). Starting from some initial state, this procedure can be carried out for all the time steps to calculate a desired motion that will achieve the prescribed  $\mathcal{L}_c^*(t)$ .

In a general scenario where the airfoil has both pitch and heave degrees of freedom, multiple solutions exist for Eq. (20). In other words, a prescribed  $\mathcal{L}_c^*$  variation can be generated using a pure heave motion or a pure pitch motion or using different combinations of combined pitch–heave profiles. In this work, we only consider the cases where one degree of freedom of the airfoil is prescribed or restrained, and the other can be obtained uniquely from Eq. (20).

It is useful to have a closer look at the contributions to  $\mathcal{L}^*$ . From Eqs. (4) and (8), we can see that  $\mathcal{L}^*$  can be interpreted as a sum of the following contributions from various factors:

$$\mathcal{L}^* = \mathcal{L}_\theta^* + \mathcal{L}_{\dot{\theta}}^* + \mathcal{L}_h^* + \mathcal{L}_{DV}^*, \quad (21)$$

where, for a symmetric airfoil,

$$\mathcal{L}_\theta^* = \frac{1}{\pi U_{net}} \int_0^\pi U \sin \theta d\nu = \frac{1}{U_{net}/U} \sin \theta, \quad (22)$$

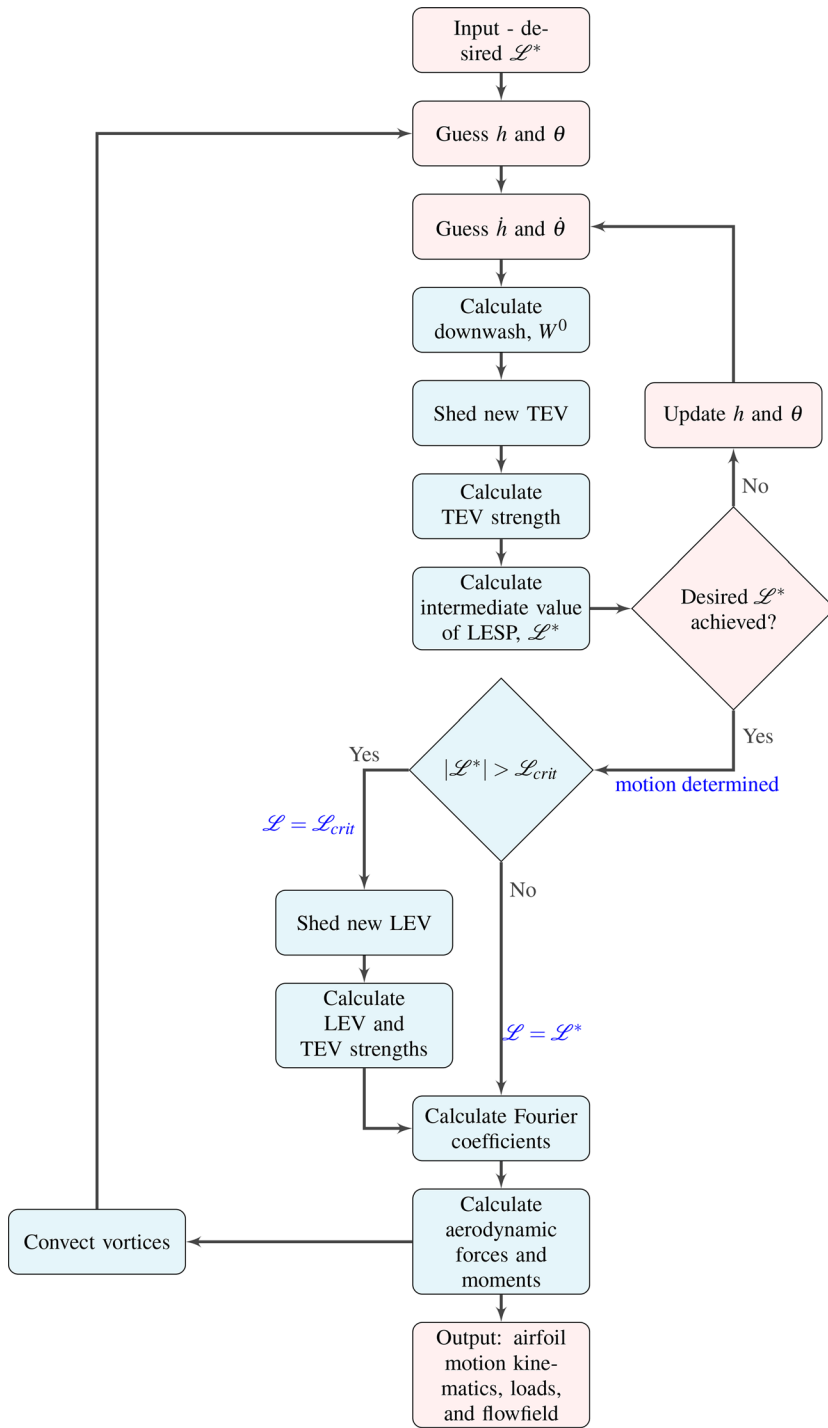
$$\begin{aligned} \mathcal{L}_{\dot{\theta}}^* &= \frac{1}{\pi U_{net}} \int_0^\pi (\dot{\theta}(x(\nu) - x_p)) d\nu \\ &= \frac{\dot{\theta} c}{U_{net}} \left( \frac{1}{2} - \frac{x_p}{c} \right) = \frac{\dot{\theta}}{U_{net}/U} \left( \frac{1}{2} - \frac{x_p}{c} \right), \end{aligned} \quad (23)$$

$$\begin{aligned} \mathcal{L}_h^* &= \frac{1}{\pi U_{net}} \int_0^\pi -\dot{h} \cos \theta d\nu \\ &= -\frac{\dot{h}}{U_{net}} \cos \theta = -\frac{\dot{h}}{U_{net}/U} \cos \theta, \end{aligned} \quad (24)$$

and

$$\mathcal{L}_{DV}^* = \frac{1}{\pi U_{net}} \int_0^\pi w_{ind}(\nu) d\nu. \quad (25)$$

Figure 5 shows the flow chart of the inverse-aerodynamic formulation algorithm. The algorithm receives a prescribed  $\mathcal{L}^*$  variation as



the input and generates a kinematic profile that the airfoil needs to execute in order to achieve that  $\mathcal{L}^*$  variation. It is similar to the flow chart of the original LDVM algorithm. The new components are marked in a different color to highlight the differences. At each time step  $j$ , Eq. (20) is solved using an iterative procedure to determine the

FIG. 5. Flowchart for the inverse LDVM algorithm. Modifications to the LDVM algorithm are shown in a different color.

motion-parameter value at time  $(j+1)$ : either the pitch angle,  $\theta_{(j+1)}$ , or the heave displacement,  $h_{(j+1)}$ . Based on the guess values for these variables, the corresponding velocities  $\dot{\theta}_{(j+1)}$  and  $\dot{h}_{(j+1)}$  are calculated using a first-order backward-difference scheme. The nascent TEV is placed relative to the guessed position of the airfoil. The strengths and positions of all other DVs in the flowfield are available. Using this information, and the guess value of the kinematic state, the strength of the new TEV is determined using Eq. (7). The downwash,  $W$ , obtained using Eq. (4), along with  $U_{net}$ , obtained using Eq. (9), can be used to calculate the  $\mathcal{L}^*$  using Eq. (8). For any guess value of  $\theta_{(j+1)}$  and/or  $h_{(j+1)}$ , the left-hand side of Eq. (20) can thus be calculated. In the iterative procedure, the guess values are updated until Eq. (20) is satisfied to within a specified tolerance. In this work, MATLAB's *fsove* function is used to solve Eq. (20). Once the kinematic state is obtained, the simulation proceeds similar to the LDVM algorithm.

Equation (20) that is solved at each time step in this full inverse method is especially nonlinear because of the influence of the DVs through the  $\mathcal{L}_{DV}^*$  term, which is the cumulative effect of the incremental contribution from each DV in the flowfield to the  $\mathcal{L}^*$  and can be expressed as follows:

$$\mathcal{L}_{DV}^* = \sum \frac{1}{\pi U_{net}} \int_0^\pi w_{ind}^k(\nu) d\nu, \quad (26)$$

where the summation is taken over all the DVs in the flowfield, and  $w_{ind}^k$  is the normal velocity induced along the airfoil chord by the  $k$ th DV. From Eq. (5), we can see that

$$\mathcal{L}_{DV}^* = \sum \Gamma_k \frac{1}{\pi U_{net}} \int_0^\pi \hat{w}_{ind}^k(\nu) d\nu, \quad (27)$$

where  $\hat{w}$  is the velocity induced by a unit-strength clockwise vortex placed at the location of the  $k$ th DV. Thus, the effect of the vortices on  $\mathcal{L}^*$  can be expressed in the following form:

$$\mathcal{L}_{DV}^* = \sum \Gamma_k \hat{\mathcal{L}}_{DV,k}^*, \quad (28)$$

where  $\hat{\mathcal{L}}_{DV,k}^*$  is the contribution to  $\mathcal{L}^*$  from a unit-strength clockwise vortex placed at the location of the  $k$ th DV and is a function of the position of the vortex relative to the airfoil. Suresh Babu *et al.*<sup>44</sup> presented a graphical approach using LESP maps to visualize the contribution from the DVs to  $\mathcal{L}^*$  and thus their role in suppressing or enhancing the LEV shedding from an airfoil. Figure 6 shows the LESP map, which is a contour plot of the incremental  $\mathcal{L}^*$  due to a unit-strength clockwise DV placed at different locations around the airfoil. A clockwise vortex causes a negative  $\mathcal{L}^*$  if it is located in the leading half of the LESP map, and results in a positive  $\mathcal{L}^*$  if it is located in the trailing half. The trends are opposite for a counterclockwise vortex. Irrespective of the sense, the magnitude increases as the vortex moves closer to either edge of the airfoil. Also, the zero contour line is normal to the airfoil passing through the midchord location. The contribution to  $\mathcal{L}^*$  from each DV can be evaluated by multiplying its strength by the value of  $\hat{\mathcal{L}}_{DV,k}^*$  value due to its location on the LESP map. More details of the LESP map can be found in Suresh Babu *et al.*<sup>44</sup> The use of LESP maps and the decomposition of  $\mathcal{L}^*$  is demonstrated in Sec. IV A. Although the LESP map provides a way to visualize the effect of any DV on the  $\mathcal{L}^*$ , the calculations of  $\mathcal{L}_{DV}^*$  necessary for the full inverse method at every time step are carried out by adapting the LDVM code which already has the functions for these calculations, as illustrated in the flow chart in Fig. 5.

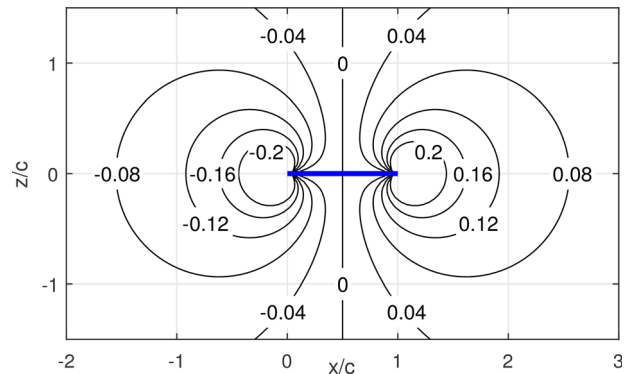


FIG. 6. LESP map for a symmetric airfoil.

## B. Simplified inverse formulation using QSTAT

It is of interest to explore a simplified, quasi-steady inverse approach in which the contributions of the DVs are ignored. The  $\mathcal{L}^*$  from this QSTAT approach can be written as follows:

$$\begin{aligned} \mathcal{L}^* &= \mathcal{L}_\theta^* + \mathcal{L}_{\dot{\theta}}^* + \mathcal{L}_h^* \\ &= \frac{1}{U_{net}/U_{ref}} \left[ \sin \theta + \dot{\theta} \left( \frac{1}{2} - \frac{x_p}{c} \right) - h^* \cos \theta \right]. \end{aligned} \quad (29)$$

This decomposition not only provides insight into the role played by various motion parameters in the LEV shedding phenomena from the airfoil but also aids us in estimating the required motion kinematics. For example, we can see that a pitch-up motion about a pivot location that is forward of the half-chord location and starting from zero pitch angle results in an increase in the  $\mathcal{L}^*$  due to both the pitch-angle and pitch-rate terms. On the other hand, when the pivot location is aft of the half-chord location, the same pitch-up motion will result in an initial decrease in the  $\mathcal{L}^*$ , due to the pitch-rate effect, that then transitions to an increase in the  $\mathcal{L}^*$  due to the pitch-angle contribution. In contrast, the effect of heave on the  $\mathcal{L}^*$  is relatively more straightforward: a heave-up motion results in a decrease in the  $\mathcal{L}^*$  and a heave-down motion does the opposite. As another example, we can consider if a heave motion can be used to cancel the  $\mathcal{L}^*$  variation resulting from a pitch-up motion. If the pivot is forward of the half-chord location, the  $\mathcal{L}^*$  increases during the pitch-up motion. It is plausible that a heave-down motion can be found that exactly cancels this  $\mathcal{L}^*$  decrease.

The QSTAT formulation for  $\mathcal{L}^*$  can thus be used to quickly design motion kinematics that will achieve a desired  $\mathcal{L}^*$ . Such a solution will be approximate because the effects of the DVs are ignored. However, such a solution may have acceptable accuracy in situations where the effects of the DVs are small compared to the contributions from the motion parameters. For the QSTAT-based inverse design, in a manner similar to the full inverse approach, at each time step  $j$ , Eq. (20) is solved using an iterative procedure to determine either the pitch angle,  $\theta_{(j+1)}$ , or the heave displacement,  $h_{(j+1)}$ . However, rather than calculate the full flow solution using LDVM for each guess of the motion-parameter value at time  $(j+1)$ , the simplified analytical expression for  $\mathcal{L}^*$  from QSTAT, given in Eq. (29), is used. This QSTAT inverse calculation procedure is much faster than the full

inverse calculation and can be performed without the need for the LDVM code. Since QSTAT does not take into account the effect of the vortices in the flowfield, the QSTAT approach can be expected to work reasonably well in cases where the effect of vortices on  $\mathcal{L}^*$  is not significant. As we will demonstrate later in Sec. V, the predictions using QSTAT is not reliable in cases with vortex-dominated flowfields.

#### IV. LEV TAILORING USING FULL INVERSE AERODYNAMIC FORMULATION

Several case studies are presented in this section to demonstrate various capabilities of the LEV tailoring algorithm and to validate its predictions using high-fidelity CFD results. In Sec. IV A, we present examples to demonstrate the capability to precisely affect the timing of the LEV formation. Section IV B has examples to illustrate the capability to generate LEVs of desired strengths. In Sec. IV C, we present the capability to generate similar LEVs using very different motion kinematics. Section IV D is used to show that it is possible to suppress LEV formation by suitable superposition of motions. In all the case studies presented here, we use a NACA0012 airfoil at a chord-based Reynolds number of 30 000 and a pivot point at the leading edge. For this airfoil- $Re$  combination, a value of 0.17 is used for  $\mathcal{L}_{crit}$  in the inverse-aerodynamic formulation.

##### A. LEV initiation and termination at prescribed time instants

Here, we demonstrate how the inverse-aerodynamic formulation can be used to initiate and terminate LEV shedding from an unsteady airfoil at prescribed time instants and thereby tailor the duration of LEV shedding from an unsteady airfoil. We first present a case with LEV shedding from only the upper surface of the airfoil and then discuss a situation with LEV shedding from both the surfaces.

###### 1. LEV shedding from one surface

Consider the commanded  $\mathcal{L}^*$  profile (red curve, left axis) shown in Fig. 7. It exhibits a top-hat profile with a maximum value of 0.20.

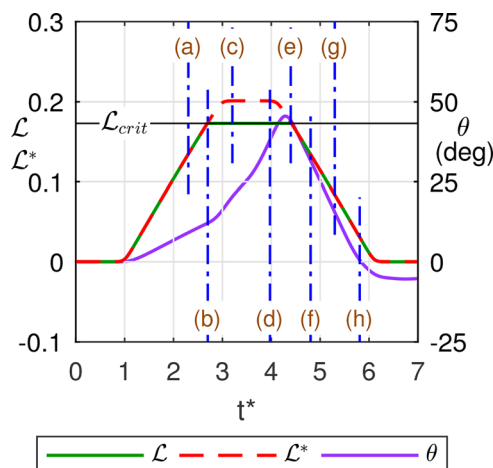
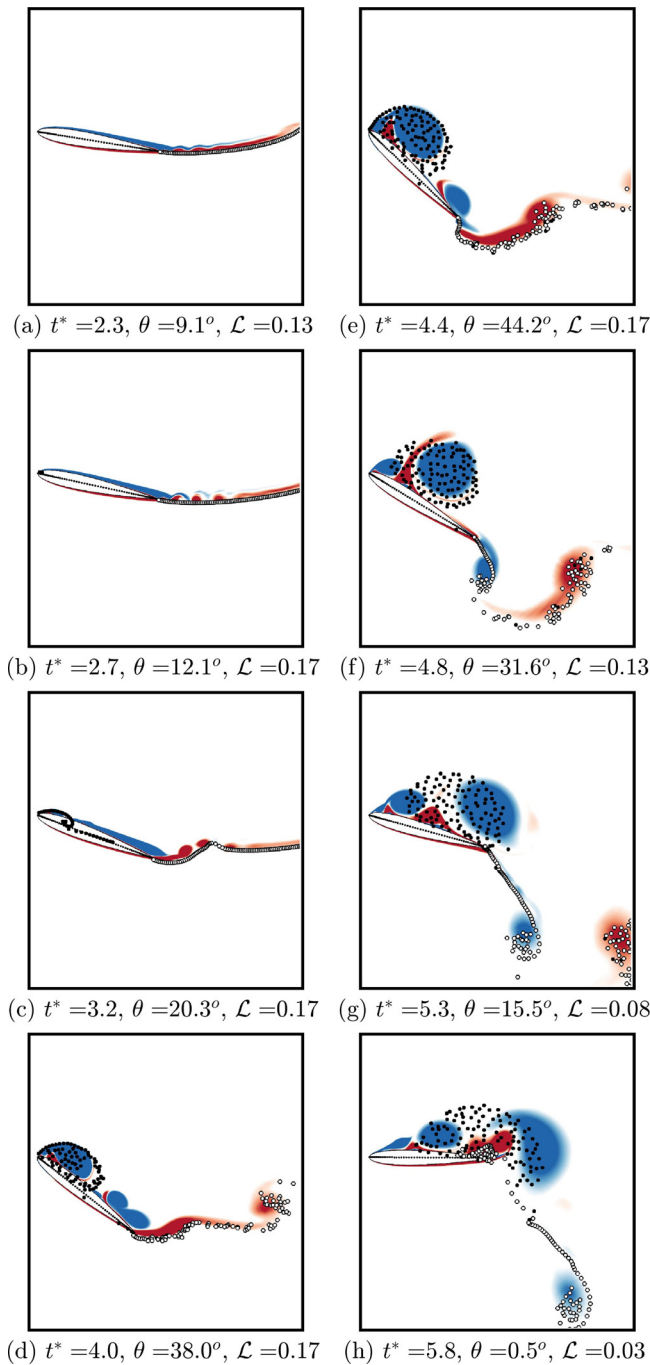


FIG. 7. Case A.1: Commanded  $\mathcal{L}^*$  curve and the resulting pitch motion and  $\mathcal{L}$  variation.

Various time instants marked on the curve will be used later in the discussion of the flowfield evolution. The commanded  $\mathcal{L}^*$  profile exceeds the critical value of  $\mathcal{L}_{crit} = 0.17$  for a finite duration of time between the two instants marked by (b) at  $t^* = 2.7$  and (e) at  $t^* = 4.4$ . Thus, the commanded  $\mathcal{L}^*$  profile is one that enforces the initiation of LEV shedding from the upper surface of the airfoil at  $t^* = 2.7$ , and the LEV termination at  $t^* = 4.4$  and thus prescribes a duration of  $1.7t^*$  between these two time instants.

Any maneuver that can achieve the commanded  $\mathcal{L}^*$  variation will result in LEV initiation and termination, respectively, at the two prescribed time instants. Here, we consider a pure pitch motion to achieve the commanded  $\mathcal{L}^*$ . Based on Eqs. (22) and (23), we can see that this can be achieved by an initial pitching-up motion followed by a pitch down motion. The pitching kinematics required to be executed by the airfoil in order to track the commanded  $\mathcal{L}^*$ , as predicted by the inverse-aerodynamic formulation, is shown using the purple curve (right axis) in Fig. 7. The resulting variation of the LESP of the airfoil,  $\mathcal{L}(t)$ , is shown using the green curve (left axis). The airfoil remains at zero pitch angle in the beginning, resulting in  $\mathcal{L}(t) = 0$ , until the commanded  $\mathcal{L}^*$  starts increasing at  $t^* = 1.0$ . The airfoil then adopts a pitch-up motion such that  $\mathcal{L}$  increases in the positive direction. As is evident from Fig. 7, the value of the pitch angle is chosen at every time step such that the resulting  $\mathcal{L}$  equals the commanded  $\mathcal{L}^*$ . This holds true until  $t^* = 2.7$  at which point  $\mathcal{L}^*$  exceeds  $\mathcal{L}_{crit}$ , marking the initiation of LEV shedding. The flow images for this case at the eight time instants marked in Fig. 7 are shown in Fig. 8. It is seen that a shear layer starts to emanate from the leading edge in the CFD results and DVs are being released in the LDVM results when the airfoil is at a pitch angle of about  $11^\circ$ . During this time, the  $\mathcal{L}^*$  continues to exceed  $\mathcal{L}_{crit}$ , and consequently, the  $\mathcal{L}$  is held at  $\mathcal{L}_{crit}$  through the release of discrete LEVs. The subsequent flow images show a concentrated region of vorticity developing near the leading edge while the airfoil continues to pitch up to larger pitch angles. The flow image at  $t^* = 4.0$  shows the airfoil at a large angle of  $38^\circ$  with an LEV structure that is starting to dominate the upper surface of the airfoil. As the LEV structure grows stronger it starts to lift off the airfoil surface while the feeding shear layer continues to add vorticity. The flow image at  $t^* = 4.4$  shows a mature LEV structure tethered to the leading edge via a thin shear layer. Following this time instant, the airfoil enters the pitch-down phase in order to track the decreasing  $\mathcal{L}^*$ . Soon after the airfoil starts pitching down, the discrete-LEV shedding is seen to terminate in the LDVM exactly at the predetermined time instant when  $\mathcal{L}^*$  falls below the critical value. In the CFD results, the concentrated LEV structure can be seen to get detached from the shear layer and convect downstream. Toward the end of the motion, the remnants of the feeding shear layer can be seen to reattach to the airfoil surface in the CFD images while the DV cluster from LDVM overlaps with the detached LEV structure. During this phase, a strong interaction between the clockwise LEV and the counterclockwise vorticity from the airfoil boundary layer can be seen to take place. Such viscous effects, which are impossible to model in LDVM, lead to small differences between the two methods. Nevertheless, the LEV termination event occurs in CFD at approximately the desired time instant of  $t^* = 4.4$  with reasonable accuracy.

Even though the overall nature of the pitch angle profile is a pitch-up and return motion, it can be noticed that the profile has highly nonlinear variations in pitch rate that are not intuitive. For



**FIG. 8.** Case A.1: DV plots from LDVM overlaid on vorticity contours from CFD. The respective time instants are shown in panels (a)–(h).

example, once the LEV shedding starts, the airfoil pitches up faster. Also, after starts decreasing from the maximum value, there is a small delay before the start of the pitch-down motion. Moreover, it can be noticed that the airfoil holds a small negative pitch angle at the end of the motion. These events result from the interplay between various

factors influencing  $\mathcal{L}^*$ , among which the interaction between the LEV and the airfoil is a significant one.

The interplay can be visualized by performing a decomposition of  $\mathcal{L}^*$  into various contributions, as mentioned in Eq. (21), and by using the LESP maps. The left axis of Fig. 9(a) shows the evolution of the various terms in Eq. (21) during the motion. The various terms are re-organized in Fig. 9(b) (left axis) into kinematic components and flowfield components to show how they add up to give the required  $\mathcal{L}^*$  variation. The pitch-angle variation of the airfoil is also shown on the right axis of these two figures. The LESP maps can be employed to get a better understanding of the effects of the flowfield evolution on the  $\mathcal{L}^*$  and thus the pitch angle profile determined by the inverse method. Figure 10 shows the DV distributions from LDVM at various time instants on the left column. Clockwise vortices are colored green while the counterclockwise vortices are colored magenta. Corresponding to each DV plot, a colorized LESP map is shown on the right column in which the DVs are colored according to their contribution to  $\mathcal{L}^*$ . Note that the sum of values at all points in a colorized map at any time instant is equal to the value of the blue curve in Fig. 9(b) at that time instant.

The airfoil initially sheds counterclockwise TEVs when it starts pitching up to track the increasing  $\mathcal{L}^*$ . These TEVs, located in the trailing half of the LESP map, make a small negative contribution to  $\mathcal{L}^*$  [red curve in Fig. 9(a)]. During this phase, the pitch angle

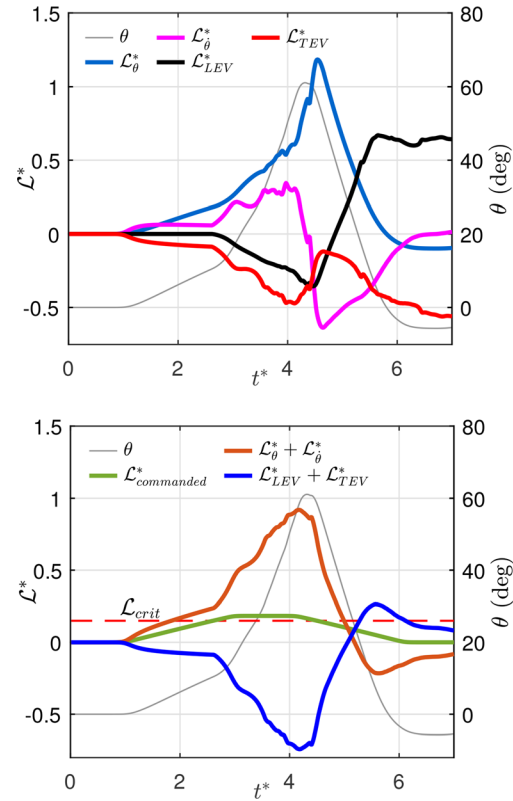


**FIG. 9.** The role of various factors governing the LEV shedding dynamics for case A.1. (a) Contribution to  $\mathcal{L}^*$  from each factor. (b) Total  $\mathcal{L}^*$  history split into contributions from kinematic factors and flowfield elements.

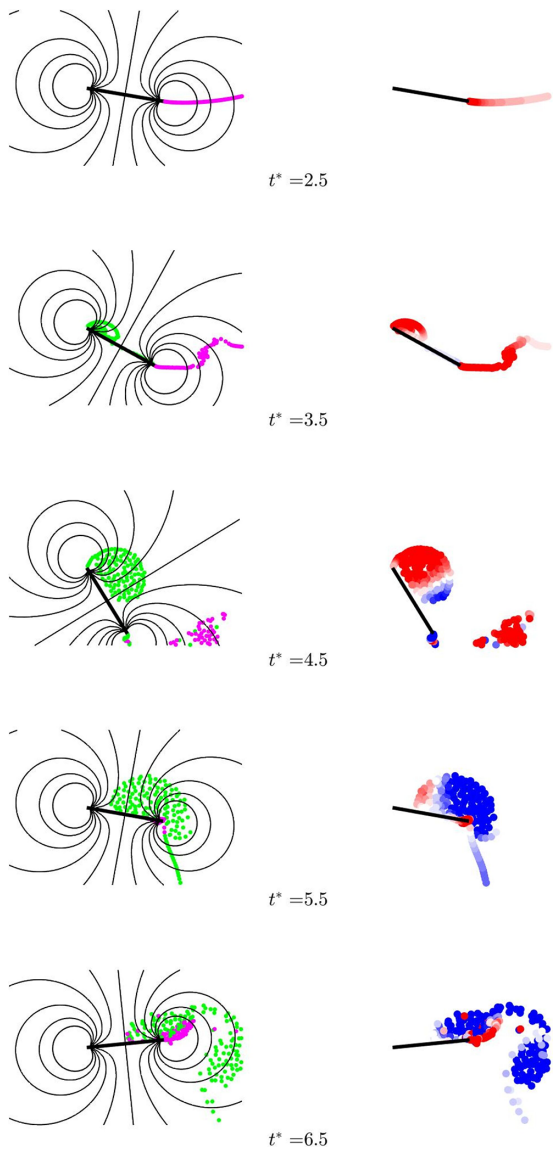


**FIG. 10.** LESP maps and colorized maps for case A.1 at various time instants. The colorized maps show the contribution to  $\mathcal{L}^*$  from individual DVs in the flowfield.

variation is chosen such that the positive pitch and pitch-rate components overcome the negative contribution from the TEVs to yield the desired positive  $\mathcal{L}^*$  in Fig. 9(b). This gradual pitching motion continues until the start of LEV shedding. After LEV initiation, the discrete LEVs start strongly affecting the flowfield contributions to the  $\mathcal{L}^*$ . The clockwise LEV, evolving in the leading half of the LESP map, causes an increasingly negative contribution. The contribution becomes strongly negative as the LEV grows in size and dominates the leading half of the LESP map. Meanwhile the contribution from the TEVs also becomes increasingly negative. The combined flowfield contribution grows to large negative values, as shown by the blue curve in Fig. 9(b). Consequently, the airfoil exhibits a somewhat aggressive

pitch-up motion during this time period so as to counteract the large negative contribution from the flowfield factors. As the LEV starts crossing into the trailing half of the LESP map, some discrete LEVs start resulting in a positive contribution, as can be seen from the colorized maps. Thus, the LEV contribution starts becoming less negative in Fig. 9(a). Meanwhile, the required  $\mathcal{L}^*$  also starts decreasing. Consequently, the airfoil adopts smaller values of pitch angle and enters the return phase. It can be seen in the colorized maps that as the LEV passes into the trailing half of the LESP map, it creates a strong positive contribution which is reflected in both Figs. 9(a) and 9(b). Thus, in terminal phase of the motion for  $t^* > 6$ , the airfoil has to adopt a slight pitch-down orientation to counteract this positive contribution from the flowfield and maintain the overall  $\mathcal{L}^*$  at zero.

It should be noted that the current pitch motion can be uniquely determined for the given commanded  $\mathcal{L}^*$ . By using a different commanded  $\mathcal{L}^*$  curve that crosses the critical value of LESP at  $t^* = 2.7$  and  $t^* = 4.4$ , LEV shedding can be achieved between these two time instants using a different pitching maneuver, which, as will be shown later in case study B.2, will result in an LEV with a different strength.

## 2. LEV shedding from both surfaces

In this case study, we demonstrate that on-demand LEV shedding can be achieved from both surfaces of the airfoil by commanding an appropriate  $\mathcal{L}^*$  profile. We demonstrate this using a pure pitch motion. The commanded  $\mathcal{L}^*$  variation for this case study is shown in Fig. 11. The pitching kinematics adopted by the airfoil to track the commanded  $\mathcal{L}^*$  profile is shown on the right axis of Fig. 11. The  $\mathcal{L}^*$  starts from zero at  $t^* = 0$  and has an increasing trend initially. It exceeds the positive critical value for a finite period of time between  $t^* = 1.5$  and  $t^* = 3.5$ . This prescription indicates that LEV shedding should occur on the upper surface of the airfoil if it adopts a kinematics to track the commanded  $\mathcal{L}^*$ . For  $t^* > 5$ ,  $\mathcal{L}^*$  continues to decrease toward negative values. Its magnitude again exceeds the critical value between  $t^* = 6.5$  and  $t^* = 8.5$ , indicating that the shedding of leading-edge vorticity should occur from the lower surface of the airfoil during this period of time. The commanded  $\mathcal{L}^*$  is in fact a

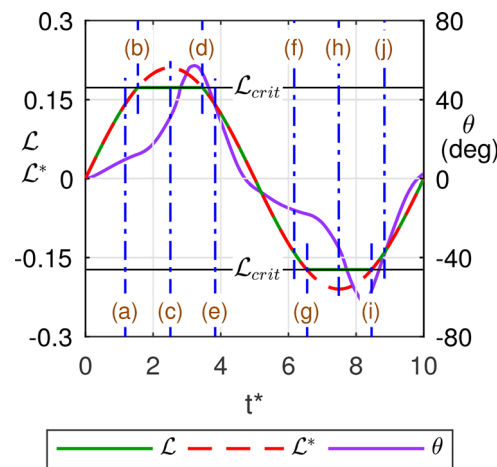


**FIG. 11.** Case A.2: Commanded  $\mathcal{L}^*$  curve and the resulting pitch motion and  $\mathcal{L}$  variation.

sinusoidal profile, and thus, the second temporal half is the mirror image of the first half. Thus, the upper- and lower-surface LEVs can be expected to be similar to each other.

The flow images for this case are shown in Fig. 12 for the ten time instants marked in Fig. 11. These images confirm that the LEV formation occurs from the two surfaces of the airfoil during the desired time periods. The flow images are selected such that the left column is from the first half of the motion and the right column is from the second half. The value of the pitch angle is also shown along with each flow image. Also, each row shows the flow images at two time instants corresponding to the same magnitude of  $\mathcal{L}^*$ , but with opposite sign. It can indeed be noticed that the flow images in Fig. 12 at the corresponding phases of  $\mathcal{L}^*$  in the two halves are qualitatively similar.

As seen from the pitch-angle variation in Fig. 11 (right axis), during the first half, the airfoil executes a pitch-up maneuver to achieve LEV shedding from the upper surface. Upon the termination of LEV shedding from the upper surface at  $t^* = 3.5$ , the first LEV gets detached from the leading edge and convects away into the wake. Meanwhile, the airfoil enters a return phase to track the decreasing  $\mathcal{L}^*$ . This motion subsequently progresses into a pitch-down phase as the commanded  $\mathcal{L}^*$  becomes negative. The pitch angle variations during the two halves are slightly different from each other because of the fact that the lingering vorticity from the first LEV affects the flowfield, unlike the first half during which the wake was essentially clean. The asymmetry in the pitch angle is prominent during the start of the second half, when the influence of the first LEV is strong. This observation can be explained using the LESP map (not shown for this case). The presence of clockwise vorticity near the trailing edge in the LESP map causes a positive contribution to  $\mathcal{L}^*$  in the second half of the motion. Thus, the airfoil has to adopt a negative pitch angle that is larger in magnitude compared to the value at the corresponding time in the first half in order to achieve the same magnitude of  $\mathcal{L}^*$ . As the first LEV convects further downstream, its influence reduces, and we can see that the pitch angle magnitudes get closer to those from the corresponding time instants in the first half. It is interesting to point out that the required pitch angle profile may reach a “steady state” if the simulation is repeated for a few cycles of  $\mathcal{L}^*$ .

## B. Tailoring the intensity of LEV shedding

The objective of the current case study is twofold. First, we demonstrate how the inverse aerodynamic formulation can be used to design motion kinematics that can be superimposed on a given baseline motion which is devoid of any LEV formation in order to induce LEV shedding. Second, we demonstrate that the inverse method can be used to tailor not only the duration of LEV shedding but also the strength of the LEV.

### 1. Inducing LEV shedding

Here, we present a case in which the current methodology is used to design motion kinematics that can be superimposed on a given baseline motion which is devoid of any LEV formation in order to induce LEV shedding. The baseline motion considered here is a low-amplitude pitch-up-return motion kinematics, shown in Fig. 13(a). The maximum pitch angle experienced by the airfoil during this motion is only  $10^\circ$ . Thus, the  $\mathcal{L}^*$  remains below the critical value

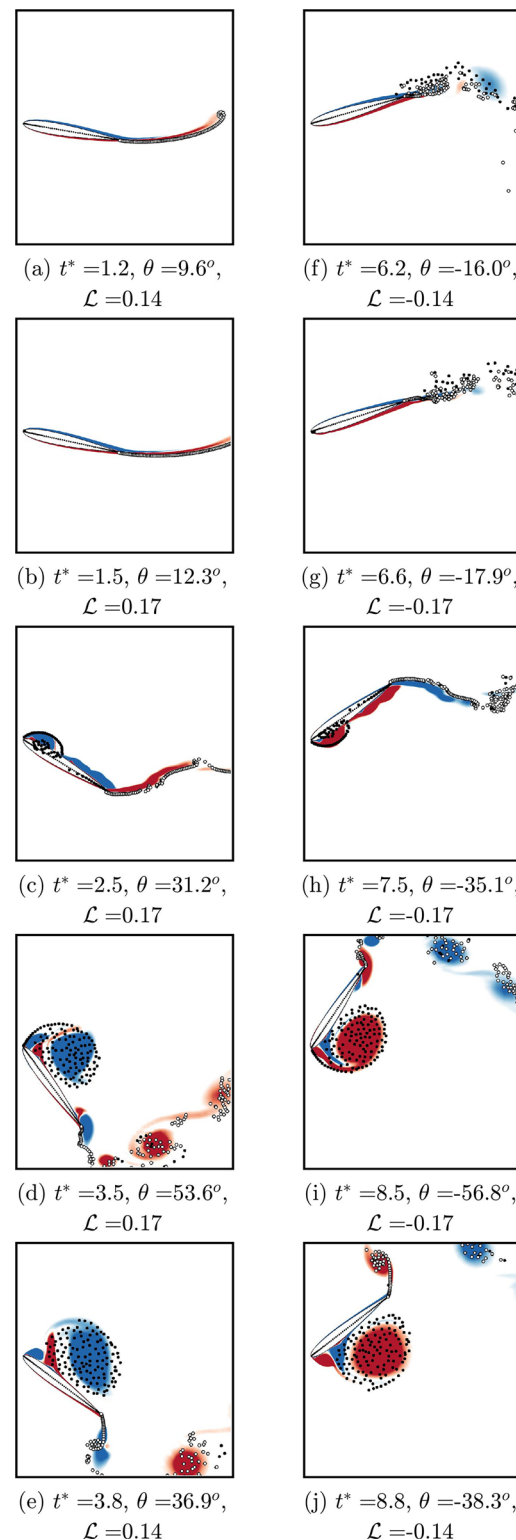
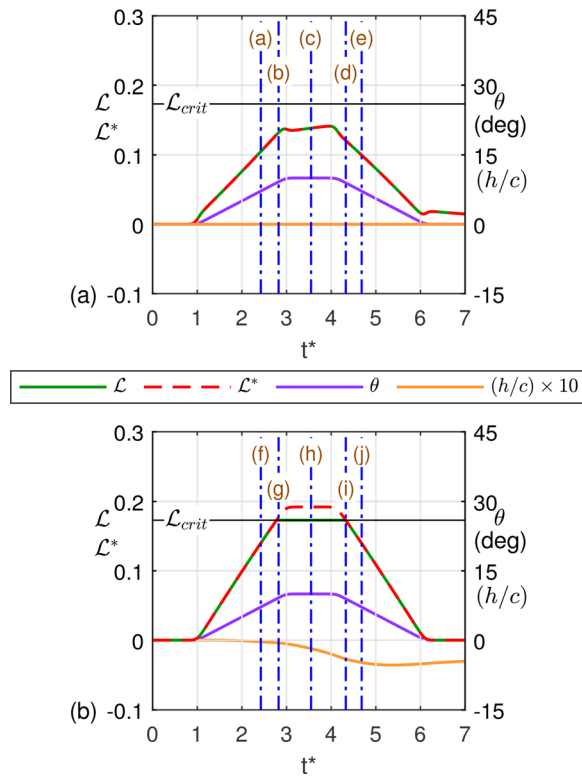


FIG. 12. Case A.2: DV plots from LDVM overlaid on vorticity contours from CFD. The respective time instants are shown in panels (a)–(j).



**FIG. 13.** Case B.1: (a) baseline pure-pitch motion and the associated  $\mathcal{L}$  and  $\mathcal{L}^*$  variations. (b) Commanded  $\mathcal{L}^*$ , the resulting heave motion, and the  $\mathcal{L}$  variation from the combined pitch-heave motion.

during the entire motion. The flow images shown in the left column of Fig. 14 confirm the absence of LEV formation during the execution of the pure-pitch kinematics.

The objective here is to design a heave motion which, when simultaneously performed along with the baseline pitch motion, will cause leading-edge vorticity to be shed from the airfoil. An example of an  $\mathcal{L}^*$  profile that can be commanded in order to achieve this objective is shown in Fig. 13(b). This  $\mathcal{L}^*$  variation exceeds the critical value for a finite time period between  $t^* = 2.8$  and  $t^* = 4.3$ . Thus, if the airfoil executes a maneuver that results in the desired  $\mathcal{L}^*$  variation, LEV shedding can be induced during this time period.

The heave motion that results in the desired  $\mathcal{L}^*$  variation can be uniquely obtained and is shown in Fig. 13(b) (right axis). The  $\mathcal{L}$  variation for the combined pitch-heave motion is also shown. As the airfoil pitches up,  $\mathcal{L}^*$  shows an increasing trend due to positive pitch-angle and pitch-rate effects. The airfoil also simultaneously executes a heave-down motion corresponding to a negative heaving velocity, which in turn causes a positive contribution to the  $\mathcal{L}^*$  according to Eq. (24). This is the main mechanism that helps the  $\mathcal{L}^*$  to be greater than its counterpart for the baseline pure-pitch motion. Thus, with the addition of the heave motion, the  $\mathcal{L}^*$  follows the commanded profile. The snapshots in the right column of Fig. 14 show the flowfield evolution for the combined pitch-heave motion. LEV shedding begins at  $t^* = 2.8$  when the  $\mathcal{L}^*$  exceeds  $\mathcal{L}_{crit}$ . The LEV can be seen to start rolling up near the leading-edge in Fig. 14(h). On continued accumulation

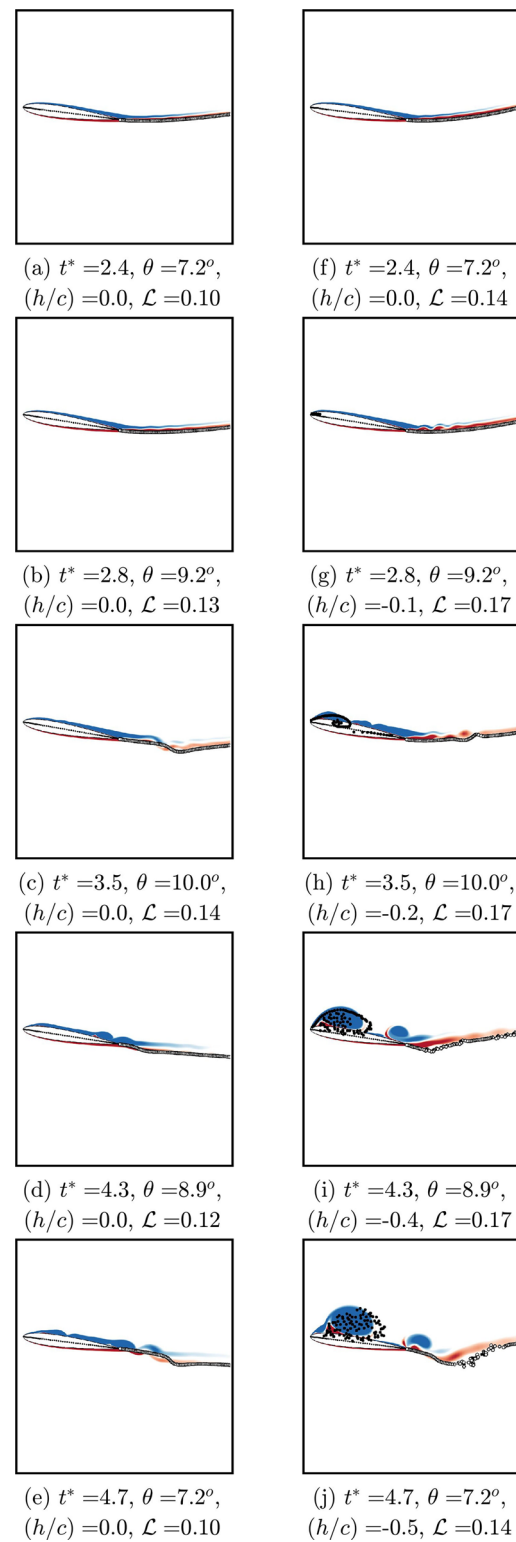


**FIG. 14.** Flow visualization for case B.1. Panels (a)–(e): flow images for the pure-pitch motion. Panels (f)–(j): flow images for the combined pitch-heave motion.

of vorticity, the LEV grows into a concentrated vortical structure. Figure 14(i) shows the matured LEV structure moving away from the airfoil surface, while still connected to the leading edge via the shear layer. LEV shedding terminates at  $t^* = 4.3$  when  $\mathcal{L}^*$  decreases below  $\mathcal{L}_{crit}$ . Following this time instant, the feeding shear layer is detached from the leading edge, as seen in Fig. 14(j), and the LEV can be seen to start convecting downstream.

## 2. Tailoring the LEV strength

Here, we demonstrate how the current inverse-aerodynamic framework can be used not only to tailor the duration of the LEV shedding but also to generate an LEV with a desired strength. It can be shown that the strength of the latest LEV at the  $i$ th time step can be approximated as follows:

$$\Gamma_{LEV}^i = c_1 \Delta \mathcal{L}^{*i} + c_2, \quad (30)$$

where  $\Delta \mathcal{L}^{*i} = \mathcal{L}^{*i} - \mathcal{L}_{crit}$ , and  $c_1$  and  $c_2$  are two constants. For continuity, the derivation of this expression is omitted here and is included in the Appendix. This expression suggests that the strength of the latest discrete LEV is proportional to the amount by which  $\mathcal{L}^*$  exceeds  $\mathcal{L}_{crit}$  at the current time step. Thus, the total strength of an LEV is determined by the area  $\mathcal{A}$  between the  $\mathcal{L}^*$  curve and the  $\mathcal{L}_{crit}$  line for the period of time between the initiation and the termination of the LEV. In other words, the strength of the LEV can be tailored by varying this area. Consider the three commanded  $\mathcal{L}^*$  curves shown in Fig. 15(a). All of them exceed  $\mathcal{L}_{crit}$  at the same time instant ( $t^* = 2.8$ ) and return below  $\mathcal{L}_{crit}$  at the same time instant ( $t^* = 4.3$ ) and have areas  $\mathcal{A}_1$ ,  $\mathcal{A}_2 = 1.5\mathcal{A}_1$ , and  $\mathcal{A}_3 = 2\mathcal{A}_1$ , respectively, above the  $\mathcal{L}_{crit}$  line. The baseline curve with the lowest value of  $\mathcal{A} = \mathcal{A}_1$  is the same as the commanded  $\mathcal{L}^*$  curve of case B.1 in Fig. 13. If the three  $\mathcal{L}^*$  curves are used to obtain heave motions to be superimposed with the baseline pitch motion in case B.1 in order to induce LEV shedding, the duration of LEV shedding will be the same for the three combined pitch–heave motions. However, the strengths of the resulting three LEVs can be expected to follow the same trend as the areas. The heaving profiles required to achieve the three  $\mathcal{L}^*$  variations are shown in Fig. 15(b) along with the baseline prescribed pitch motion. There are two factors affecting the required heave motion. First, to achieve higher values of  $\mathcal{L}^*$ , the  $\mathcal{L}_h^*$  term in Eq. (21) needs to be higher, resulting in a larger heave velocity, which eventually leads to larger heave displacements. Second, for larger values of  $\Delta \mathcal{L}^{*i}$ , the discrete LEVs released from the airfoil are stronger. Using the LESP maps, it can be visualized that the negative contribution from all the discrete LEVs to the  $\mathcal{L}^*$ , especially during the LEV maturity phase, is also higher. The heave motion needs to take into account this effect of the LEVs on the  $\mathcal{L}^*$ . Thus, the required heaving motion becomes increasingly aggressive as the value of  $\mathcal{A}$  increases as can be noticed from Fig. 15(b). Since the commanded  $\mathcal{L}^*$  curves overlap before LEV initiation, the required heave motions and hence the flow states are the same for the three cases until the instant of LEV initiation.

The evolution of the LEV for the three combined pitch–heave motions is shown in Fig. 16 for the five time instants marked in Fig. 15. The same scale has been used to plot the CFD vorticity contours for all the three cases. Thus, the strength of the LEV roughly correlates with its spatial extent. For the nominal case of  $\mathcal{A} = \mathcal{A}_1$ , in the first column, we can see a small LEV structure developing near the upper surface of the airfoil, and pinching off toward the end of the motion.

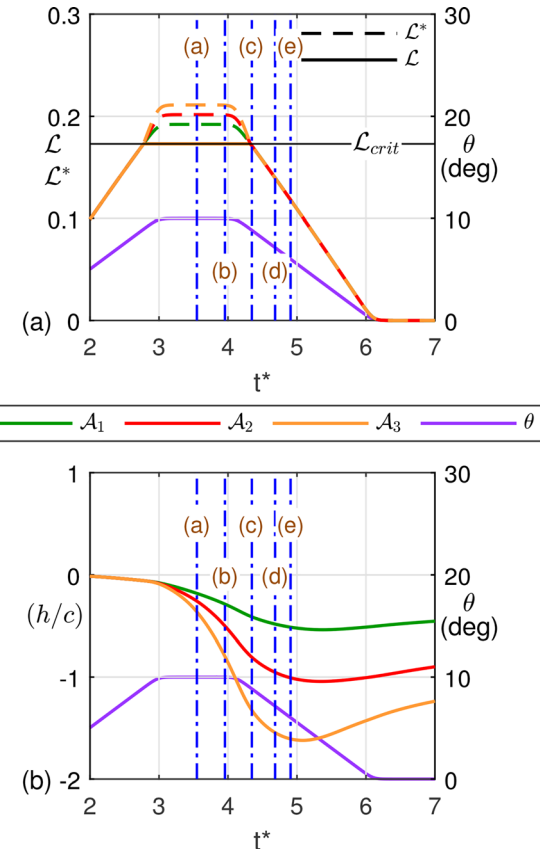
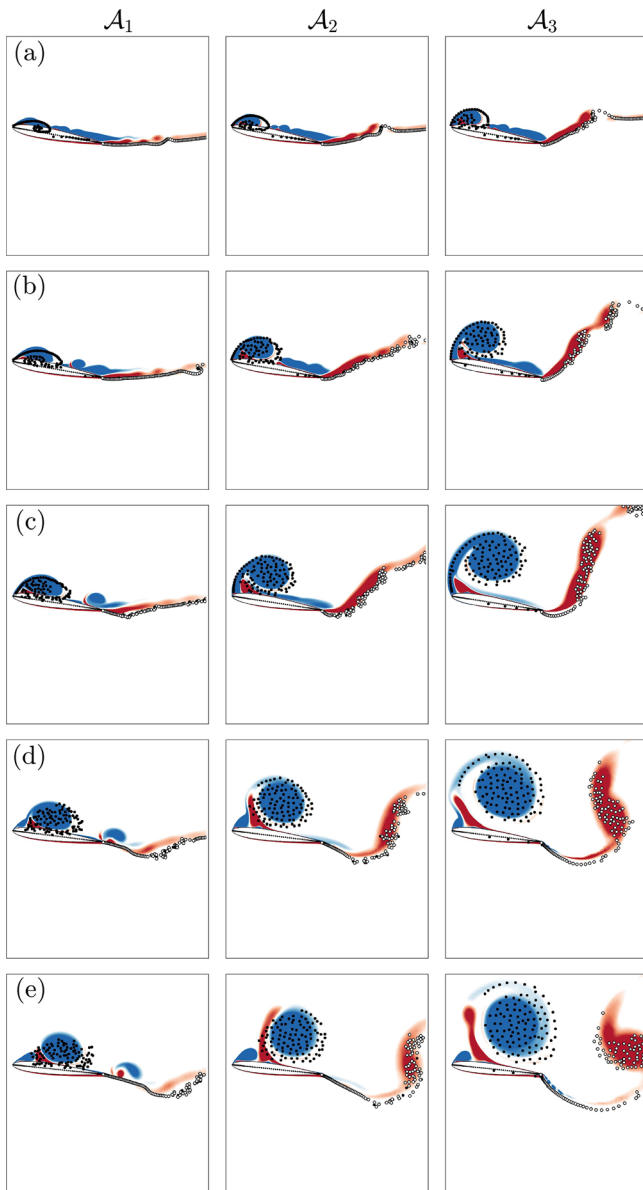


FIG. 15. Case B.2: (a) three commanded  $\mathcal{L}^*$  profiles along with the baseline pitch motion and (b) the resulting heave motions.

From a quick glance at the flow images, it can be noticed that this LEV is a rather weak one compared to the other two LEVs. For the other two motions, we can notice that at any time instant the LEV structures are larger and that the cores are farther away from the airfoil surface. Both these effects become more prominent with increasing  $\mathcal{A}$ .

The non-dimensional LEV strength,  $\hat{\Gamma} = \Gamma/(cU_{ref})$ , from both the low-order method and CFD are plotted against  $t^*$  for the three motions in Fig. 17. The LEV strength from LDVM at a particular time instant is calculated as the sum of the strengths of all the discrete LEVs present in the flowfield at that time instant. The LEV strength from CFD results is estimated using the integration of clockwise vorticity performed over the area in a box fixed in the body frame as shown in Fig. 18. As can be seen from Figs. 16 and 17, CFD results show the LEV initiation occurring in all the three motions at around the desired time instant. A steady increase in the LEV strength is seen in the results from both the methods after LEV initiation. The total LEV strengths for the three motions from the low-order method are  $\hat{\Gamma}_1 = 2.47$ ,  $\hat{\Gamma}_2 = 3.75$ , and  $\hat{\Gamma}_3 = 5.7$ , respectively, resulting in the ratios of  $\hat{\Gamma}_2 = 1.5\hat{\Gamma}_1$  and  $\hat{\Gamma}_3 = 2.3\hat{\Gamma}_1$ . This trend suggests that for moderate values of  $\mathcal{A}$ , the LEV strength can be precisely tailored using the current inverse aerodynamic formulation. The LEV strengths from CFD follow the corresponding LDVM curves very closely and level off at around the desired LEV termination time near the desired LEV strength values.



**FIG. 16.** LEV evolution for the three combined pitch–heave motions of case B.2. Rows (a)–(e) correspond to the time instants marked in Fig. 15.

Note that only a qualitative comparison of the trends from CFD is intended here using the rough estimate of the circulations from the CFD results. While a rigorous computation of the circulations may possibly improve the accuracy of the CFD-based circulation plots as well as the general agreement between CFD and low-order results, it can be expected that the trends will remain the same.

### C. Achieving similar LEV shedding using different motions

In this case study, we show that the LEV shedding pattern from an airfoil undergoing a prescribed pure pitching motion can be

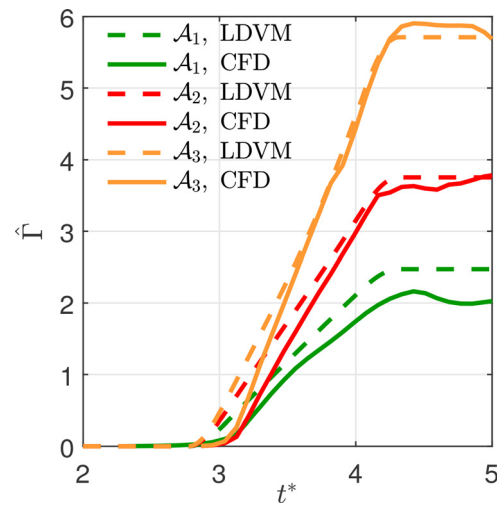


**FIG. 17.** Case B.2: Variations of LEV strength for the three combined pitch–heave motions.

replicated using a corresponding pure heaving motion. In the baseline motion, the airfoil undergoes a  $0^\circ$ – $25^\circ$ – $0^\circ$  pitch-up–hold–return maneuver as shown in Fig. 19(a) on the right axis. The  $\hat{\mathcal{L}}^*$  variation resulting from this motion and the corresponding  $\hat{\mathcal{L}}$  variation are also shown (left axis).  $\hat{\mathcal{L}}^*$  is higher than critical value between  $t^* = 1.9$  and  $t^* = 4.4$ , indicating uninterrupted LEV shedding from the airfoil during this time interval. The initiation of LEV shedding takes place during the pitch-up phase, under the combined influence of the pitch rate and the pitch angle. During the hold phase, the high pitch angle of  $25^\circ$  is sufficient to sustain the LEV shedding. Soon after the airfoil enters the return phase, the reduction in pitch angle as well as the pitch

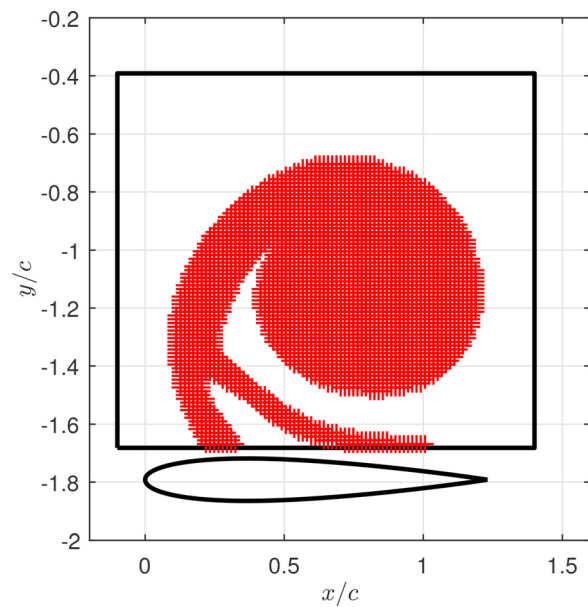


**FIG. 18.** Contour used for estimating the LEV circulation from CFD results.

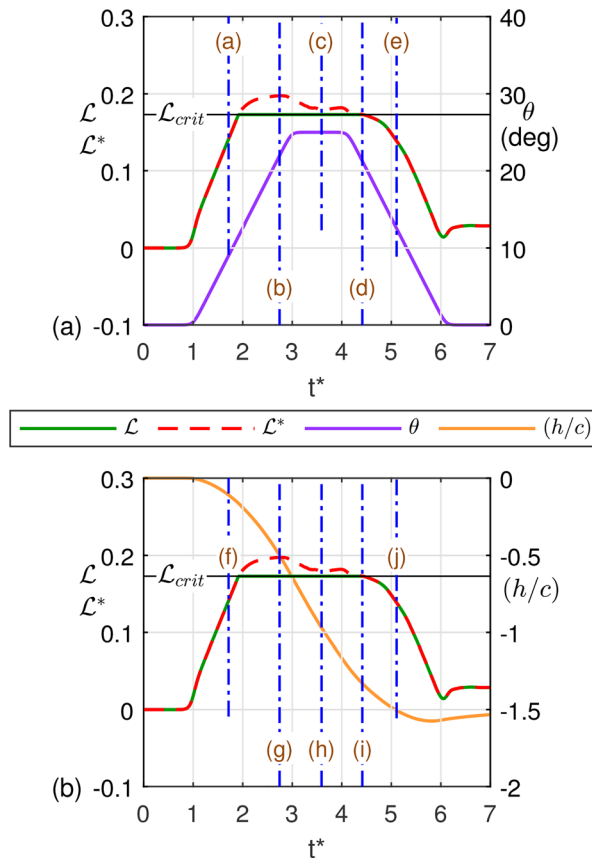


**FIG. 19.** Case C: (a) Baseline pure-pitch motion and the resulting  $\mathcal{L}$  and  $\mathcal{L}^*$  variations. (b) Pure-heave motion that generates the same  $\mathcal{L}$  and  $\mathcal{L}^*$  variations.

velocity causes  $\mathcal{L}^*$  to drop below the critical value leading to the termination of the LEV shedding. The flow images for this motion, shown in the left column of Fig. 20, confirm the initiation, development, and termination of a single LEV structure during the execution of the kinematics.

The  $\mathcal{L}^*$  variation resulting from the pitching motion in Fig. 19(a) is now used as the commanded  $\mathcal{L}^*$  to design a pure heave motion that will exhibit LEV shedding pattern similar to that of the pure-pitch motion. The heave kinematics, predicted by the inverse-aerodynamic formulation, that achieves the same  $\mathcal{L}^*$  variation as the pitching motion is shown in Fig. 19(b). It can be noticed that the airfoil executes a heave-down motion, so as to emulate the pitch and pitch-velocity effects on  $\mathcal{L}^*$  during the pitching motion. Since the  $\mathcal{L}^*$  variation and thus the resultant  $\mathcal{L}$  history are the same between the two motions, the instants of LEV initiation and termination will be the same for the two maneuvers. Moreover, continuous LEV shedding is expected to occur from the upper surface of the heaving airfoil between  $t^* = 1.9$  and  $t^* = 4.4$ , resulting in a single LEV structure. The flow images for the heave motion are shown in the right column of Fig. 20 for the five time instants marked in Fig. 19(b). The images are chosen such that in each row, the time instant and hence the value of  $\mathcal{L}^*$  are the same for the two motions. A comparison of the flow-fields reveals a qualitative similarity between the two motions in terms

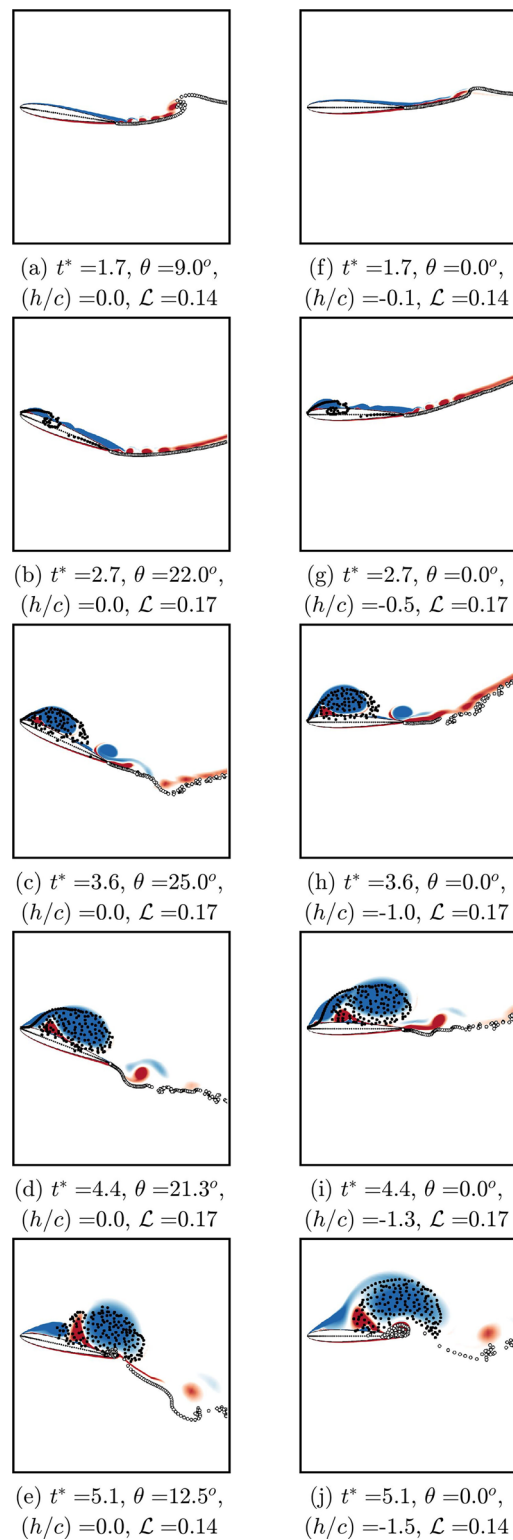


**FIG. 20.** LEV evolution for case C. Panels (a)–(e): flow images for the reference pure-pitch motion. Panels (f)–(j): flow images for the equivalent pure-heave motion.

of the topology of the vortical structures. The timings of LEV initiation and termination for the inverse-designed heave motion are reasonably close to the corresponding ones for the given pitch motion. At all stages of the development of the LEV structure, the spatial extent of the LEV can be observed to be similar between the two motions. In addition, the features such as the downstream convection of the matured LEV structure while being tethered to the leading edge by a feeding shear layer [Figs. 20(d) and 20(i)] have also been closely replicated by the heave motion. The flowfield evolution close to LEV termination are somewhat different, however. The shed LEV interacts with the trailing edge and the trailing-edge vorticity differently for the two scenarios, even in the low-order simulations. It remains to be explored whether this interaction can be tailored using an extension of the current inverse-design approach.

The non-dimensional LEV strength from both the CFD and the low-order simulations is plotted against  $t^*$  for the two motions in Fig. 21. In the low-order results, the LEV initiation and termination events occur at exactly the same time instants for the two motions. While these events have not been precisely identified for the CFD simulations in this study, reasonable estimates can be obtained from the flow images of Fig. 20 and the circulation plots of Fig. 21. It can be noticed from Fig. 21 that the LEV strengths for the two motions are close during the early phase of the motions (until about  $t^* = 3.5$ ) and diverge afterwards. The same trend is observed in both the methods.

#### D. Suppressing LEV shedding

In this case study, we seek a strategy to suppress the LEV shedding from a pitching airfoil. This aim is achieved by determining a heave motion which, when superimposed on the given prescribed pitch profile with LEV shedding, curtails the LEV shedding from the airfoil. The baseline pure-pitch motion, shown in Fig. 22(a), is the same as the pure-pitch motion used in case C ( $0^\circ$ – $25^\circ$ – $0^\circ$  pitch-up–hold–return motion about the leading edge). For this motion, LEV shedding is initiated at  $t^* = 1.9$  and is terminated at  $t^* = 4.4$ . To curb the LEV shedding, we now add a heave motion to this pitch

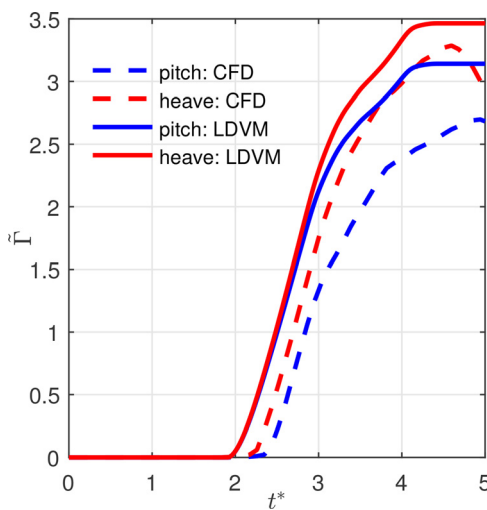


FIG. 21. Case C: LEV strength variation for the pitch motion and the heave motion.

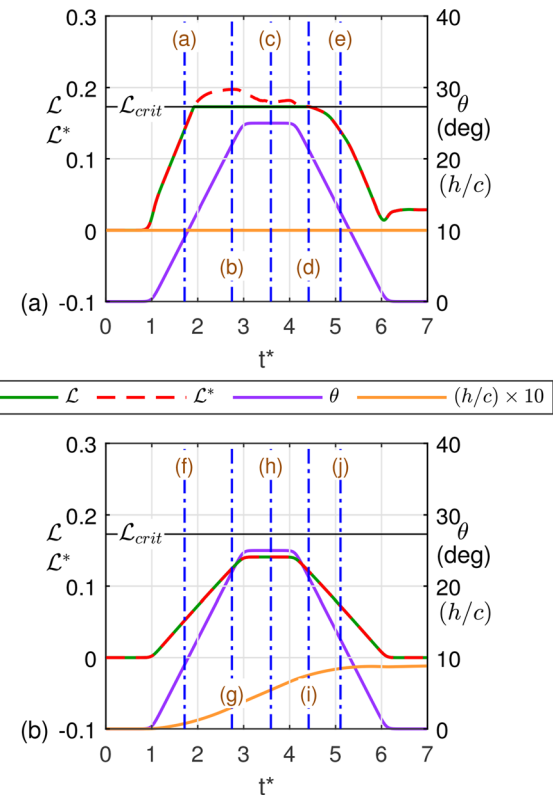
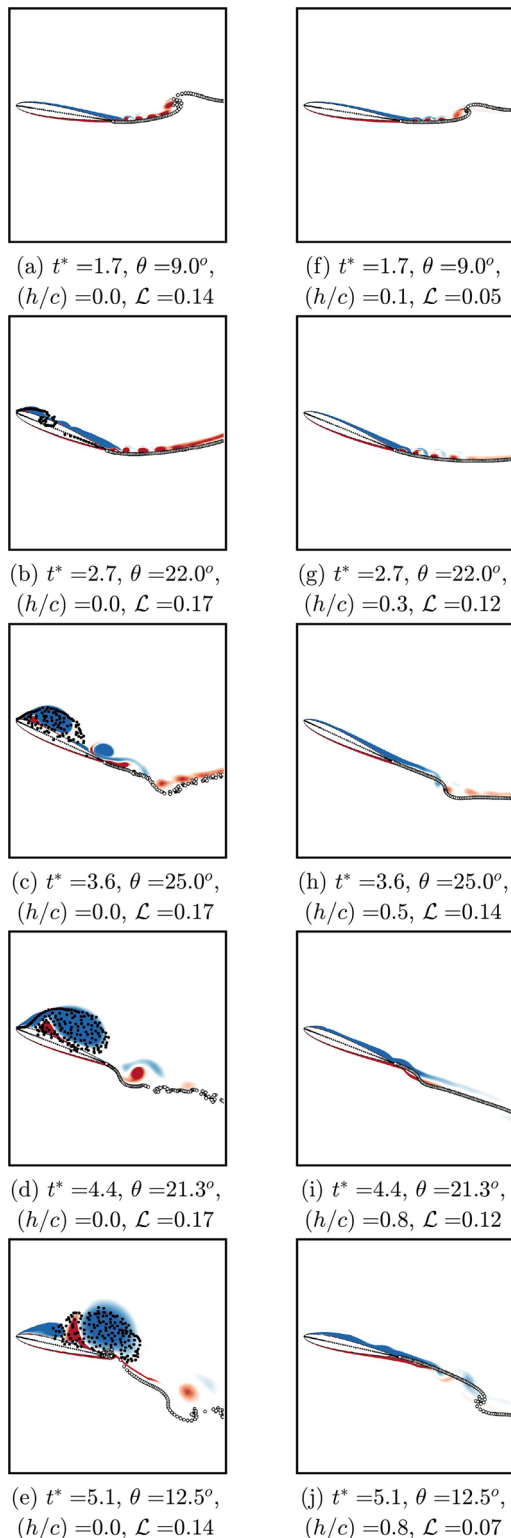


FIG. 22. Case D: (a) Baseline pure-pitch motion and the associated  $\mathcal{L}$  and  $\mathcal{L}^*$  variations. (b) Commanded  $\mathcal{L}^*$ , the resulting heave motion, and the  $\mathcal{L}$  variation from the combined pitch–heave motion.

motion. Figure 22(b) shows the commanded  $\mathcal{L}^*$  that is to be achieved by performing an appropriate heave kinematics simultaneously with the pitching maneuver. This  $\mathcal{L}^*$  does not reach the critical value at any point, and hence, the combined pitching and heaving motion should not result in any sort of LEV formation on the airfoil. The heave profile necessary to achieve the commanded  $\mathcal{L}^*$ , as calculated using the inverse formulation, is shown on the right axis of Fig. 22(b). As the airfoil executes the pitching motion, the airfoil also heaves upward. During the pitch-up phase, both the positive pitch angle and the positive pitch velocity contributions tend to increase the  $\mathcal{L}^*$ . This is counteracted by the negative contribution to the  $\mathcal{L}^*$  from the positive heave velocity. Thus, the heaving component helps to limit the increase in  $\mathcal{L}^*$  unlike what happens in the pure-pitching motion. It can also be noticed that the heaving continues to slow down as the airfoil enters the return phase. During this time period, the pitch-velocity contribution is negative, and the pitch-angle contribution continuously decreases. Both these effects cause the required counter-action from the heave velocity to decrease as the pitch-down phase progresses. The flowfield evolutions for the pure pitch motion and the combined pitch–heave motion are shown in the left and right columns, respectively, of Fig. 23. The two images in each row correspond to the same time instant. The flow images confirm the suppression of the LEV formation from the pitching airfoil by the superposition of the heaving motion.



**FIG. 23.** Flow visualization for case D. Panels (a)–(e): flow images for the pure-pitch motion. Panels (f)–(j): flow images for the combined pitch–heave motion.

While the heave profile executed in this case can be uniquely determined to achieve the commanded  $\mathcal{L}^*$ , multiple options exist for the commanded  $\mathcal{L}^*$  that will suppress LEV formation. Any commanded  $\mathcal{L}^*$  profile that does not exceed the critical value can be used to design a heave motion that achieves this objective. If the heave contribution is sufficiently high, an airfoil that is pitching up can even generate LEVs from the lower surface by commanding an  $\mathcal{L}^*$  that exceeds the critical value in the negative direction.

#### V. LEV TAILORING USING QSTAT

In this section, we assess the effectiveness of QSTAT (from Sec. III B) in designing motion kinematics and compare the predicted motion with that from the more complex full inverse approach. Consider case study C in which the  $\mathcal{L}^*$  variation from a pitch motion in Fig. 19(a) is used to design a heave motion that results in a similar LEV shedding pattern. As seen earlier in Fig. 20, the full inverse method was successful in calculating a pure-heave motion that resulted in a large LEV structure similar to the pure-pitch motion. Now, we use the QSTAT to predict the required heave motion to generate this  $\mathcal{L}^*$  variation. The heave motion predicted by QSTAT is shown in Fig. 24 along with the one predicted by the full inverse approach [from Fig. 19(b)]. Surprisingly, even though the pitch motion results in a large LEV and the simpler QSTAT approach does not take the effects of DVs into account, the heave motion predicted by QSTAT is close to that predicted by the full inverse method. In this particular case, both the pitch and heave motions have similar evolution of LEVs (both in strength and location). The effects of the LEV on the airfoil flow for either motion is similar, resulting in a cancellation of the effects when comparing the pitch and heave motions. Because the LEV contributions are ignored in both motions, the QSTAT prediction is surprisingly good for this case.

The use of QSTAT for motion design does not always result in correct predictions. For instance, when QSTAT is used to generate the motion for a prescribed  $\mathcal{L}^*$  which results in a strong LEV, the method will yield poor predictions because ignoring the DV effects results in a

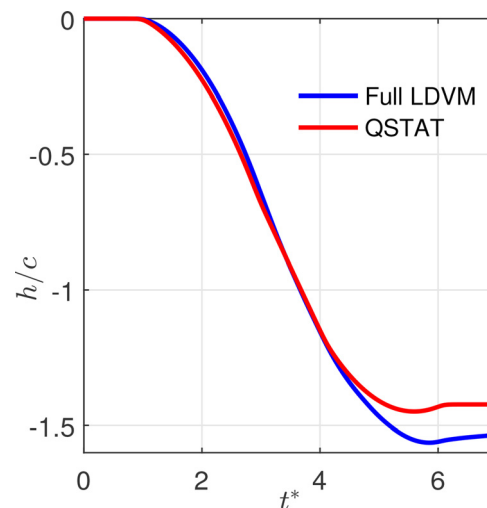


**FIG. 24.** Comparison of predictions by QSTAT and the full inverse approach for case C.

serious omission that does not get canceled like in the previous example. To illustrate this situation, we use QSTAT to design the kinematics for the commanded  $\mathcal{L}^*$  from Fig. 7 for case study A.1. The pitch motion predicted by QSTAT is shown in Fig. 25 along with the one from Fig. 7 predicted by the full model. The QSTAT prediction completely deviates from the full-model prediction, pointing to the limitation of the simpler QSTAT approach and highlighting the need for the full inverse approach.

## VI. CONCLUSIONS

This paper presents an inverse-aerodynamic algorithm to tailor the LEV shedding from an unsteady airfoil. A suitable pitching or heaving profile is determined for the airfoil to tailor the initiation, termination, and strength of LEVs shed from the unsteady airfoil. The algorithm builds upon the LDVM, which combines a large-angle unsteady theory and a discrete-vortex method, and uses the LESp to predict LEV shedding and the resultant unsteady loads on airfoils undergoing prescribed motion kinematics.

The LDVM is modified in the current work to determine a suitable motion kinematics for an airfoil in order to achieve a desired LEV shedding pattern. The desired LEV shedding pattern is supplied as input to the inverse algorithm in terms of a prescribed time variation of an intermediate value of LESp, denoted by  $\mathcal{L}^*$ . The algorithm then calculates the required pitch or heave position of the airfoil at every time step through an iterative process using the unsteady thin-airfoil theory and the discrete-vortex method. Excellent comparison is seen with high-fidelity CFD simulations of the predicted maneuvers for several case studies. Although all the case studies presented here are for symmetric airfoils, the inverse approach can also be used for cambered airfoils to design motion kinematics to achieve a user-supplied  $\mathcal{L}^*$  variation.

A given LESp variation can in fact be achieved using different combinations of pitch and heave motions. Thus, multiple solutions exist for the kinematics required to achieve a given commanded LESp variation. In this work, we have considered situations where the only one of the degrees of freedom is to be determined while the other is

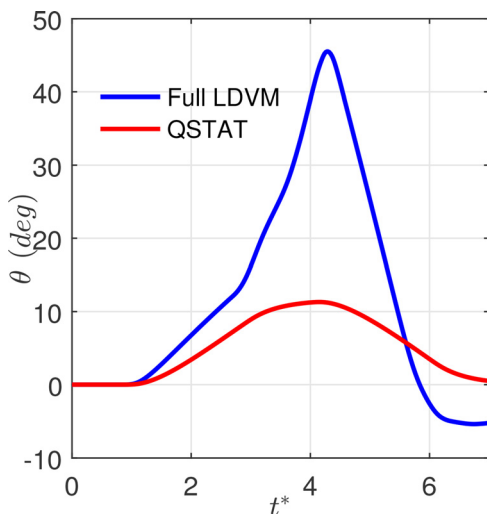


FIG. 25. Comparison of predictions by QSTAT and the full inverse approach for case A.1.

known. A unique suitable kinematic profile can then be obtained for a given LESp variation by solving a nonlinear equation in one variable. The inverse formulation, however, has no implicit constraints on the kinematics, allowing for the future addition of a capability in which the problem may be posed as a two-variable minimization problem subject to kinematic constraints for the aforementioned scenarios. While the predicted motion profile is not guaranteed to be smooth, all the profiles observed during this study were smooth. The motions predicted by the inverse aerodynamic algorithm were simulated using CFD without any modifications.

The  $\mathcal{L}^*$  profiles used in the case studies presented here were inspired by the typical  $\mathcal{L}^* - t^*$  variations that we have observed in our previous studies involving LDVM simulations of unsteady airfoils. We believe that the inverse algorithm will be able to generate motion profiles to achieve complex  $\mathcal{L}^*$  variations such as a sawtooth profile. However, the resulting motion may possibly be non-smooth and thus non-realizable for practical purposes. The current unsteady airfoil theory assumes a flow from the leading edge to the trailing edge and is hence not valid for pitch angles greater than  $90^\circ$ . Commanding  $\mathcal{L}^*$  values that are too high in magnitude (perhaps in an attempt to generate extremely strong LEVs) for designing a pitching motion may cause the resulting pitch-angle magnitude predicted by the inverse formulation to exceed  $90^\circ$ . This issue can be overcome by implementing an aerodynamic model that is valid for airfoils in reversed flows. Both the above concerns can be addressed by posing the inverse design as a minimization problem instead of a root finding problem, and adding constraints on maximum allowable position, velocity, or acceleration as desired. Regardless of the problem formulation, the LDVM or QSTAT can used as a guide to decide reasonable  $\mathcal{L}^*$  profiles for the inverse algorithm.

In this work, the strength of a discrete LEV is determined using the hypothesis (Ramesh *et al.*<sup>37</sup>) that LESp remains constant at a critical value during LEV shedding. This assumption works well for low Reynolds numbers ( $Re \approx 30\,000$ ). Recent research has shown that a noticeable drop in LESp occurs during LEV shedding at higher Reynolds numbers ( $Re > 1 \times 10^6$ ). Future extensions of the inverse formulation to these higher Reynolds numbers will need to account for this LESp drop using CFD/experimental information. For the Reynolds numbers considered in this work, as demonstrated by the case studies presented here, the predictions of the inverse algorithm shows excellent agreement with CFD simulations.

## ACKNOWLEDGMENTS

The authors gratefully acknowledge the funding support for this research from the National Science Foundation (Award No. CMMI-2015983; Program Officer: Dr. Robert Landers) and the US Air Force Office of Scientific Research (Grant FA 9550-17-1-0301; Program Managers: Dr. Gregg Abate and Dr. Douglas Smith). The authors are also grateful to Dr. Jack Edwards of North Carolina State University for the REACTMB-INS code used for the computations in this effort.

## AUTHOR DECLARATIONS

### Conflict of Interest

The authors have no conflicts to disclose.

## DATA AVAILABILITY

The data that support the findings of this study are available from the corresponding author upon reasonable request.

## APPENDIX: STRENGTH OF THE LEV

Consider a time step  $i$  during which LEV shedding is active and  $\mathcal{L}^{*i} > \mathcal{L}_{crit}$ . The strengths of the latest LEV and TEV, denoted by  $\Gamma_{LEV}^i$  and  $\Gamma_{TEV}^i$ , respectively, can be determined using the Kelvin condition and the condition that LESP,  $\mathcal{L}$ , is maintained at its critical value,  $\mathcal{L}_{crit}$ . This results in the simultaneous solution of the following system equations

$$\begin{bmatrix} 1 + \hat{\Gamma}_{B,TEV}^i & 1 + \hat{\Gamma}_{B,LEV}^i \\ \hat{\mathcal{L}}_{TEV}^i & \hat{\mathcal{L}}_{LEV}^i \end{bmatrix} \begin{Bmatrix} \Gamma_{TEV}^i \\ \Gamma_{LEV}^i \end{Bmatrix} = \begin{Bmatrix} \Gamma_B^{i-1} - \Gamma_{B,o}^i \\ \mathcal{L}_{crit} - \mathcal{L}_o^i \end{Bmatrix}, \quad (A1)$$

where the bound circulation  $\Gamma_B^i$  and  $\mathcal{L}^i$  at the current time step have been decomposed into the contributions from the various sources.  $\hat{\Gamma}_{B,TEV}^i$  and  $\hat{\Gamma}_{B,LEV}^i$  are the contributions to the bound circulation from clockwise unit-strength DVs placed at the locations of the latest TEV and LEV, respectively, while  $\Gamma_{B,o}^i$  is the combined contribution from all the other sources such as the airfoil kinematics and the other DVs (previously shed from the airfoil) in the flowfield. The quantities  $\hat{\mathcal{L}}_{TEV}^i$ ,  $\hat{\mathcal{L}}_{LEV}^i$ , and  $\mathcal{L}_o^i$  are similarly defined for the contributions to  $\mathcal{L}^i$ . Note that all the quantities with a  $\hat{\cdot}$  depend only on the locations of the latest shed vortices. The solution yields

$$\Gamma_{LEV}^i = p(\mathcal{L}_{crit} - \mathcal{L}_o^i) - q(\Gamma_B^{i-1} - \Gamma_{B,o}^i), \quad (A2)$$

where  $p$  and  $q$  are functions of only the locations of the latest shed vortices. Now,  $\mathcal{L}^*$  at the current time step can be obtained as follows:

$$\mathcal{L}^{*i} = \mathcal{L}_o^i + \mathcal{L}_{TEV*}^i = \mathcal{L}_o^i + \Gamma_{TEV*}^i \hat{\mathcal{L}}_{TEV}^i, \quad (A3)$$

where  $\mathcal{L}_{TEV*}^i$  is the contribution from the latest TEV, based on its intermediate strength,  $\Gamma_{TEV*}^i$ , which is initially calculated (by assuming that LEV shedding is absent) using the Kelvin condition as

$$\Gamma_{TEV*}^i = \frac{\Gamma_B^{i-1} - \Gamma_{B,o}^i}{1 + \hat{\Gamma}_{B,TEV}^i}. \quad (A4)$$

Using Eqs. (A3) and (A4) in Eq. (A2), we get

$$\Gamma_{LEV}^i = p\Delta\mathcal{L}^{*i} + r(\Gamma_{B,o}^i - \Gamma_B^{i-1}), \quad (A5)$$

where  $\Delta\mathcal{L}^{*i} = \mathcal{L}^{*i} - \mathcal{L}_{crit}$  and  $r$  is a function of the locations of the latest LEV and TEV. By decomposing  $\Gamma_{B,o}^i$  and applying Kelvin condition to  $\Gamma_B^{i-1}$ , the quantity inside the parenthesis can be easily shown to result from the airfoil kinematics and all the DVs in the flowfield at the current time step.

The above equation shows that the strength of the latest LEV is proportional to the amount by which  $\mathcal{L}^*$  exceeds  $\mathcal{L}_{crit}$  at the current time step. All the other quantities on the right side are influenced by the flowfield evolution and hence indirectly by the values of  $\Delta\mathcal{L}^*$  in the previous timesteps. Hence, strictly speaking, the relationship between  $\Gamma_{LEV}^i$  and  $\Delta\mathcal{L}^{*i}$  is nonlinear. The quantities  $p$  and

$r$  depend only on the location of the latest LEV and TEV, which do not vary much between timesteps. However, based on several LDVM simulations, it is observed that Eq. (A5) can be approximated by a straight-line fit:

$$\Gamma_{LEV}^i = c_1\Delta\mathcal{L}^{*i} + c_2, \quad (A6)$$

where  $c_1$  and  $c_2$  are constants. This implies that the total strength of an LEV, which is the cumulative sum of all the discrete LEVs shed during a time period when LEV shedding is active, can now be tailored by varying the area under the  $\Delta\mathcal{L}^*$  curve.

## REFERENCES

- <sup>1</sup>J. D. Eldredge and A. R. Jones, "Leading-edge vortices: Mechanics and modeling," *Annu. Rev. Fluid Mech.* **51**, 75–104 (2019).
- <sup>2</sup>W. J. McCroskey, "The phenomenon of dynamic stall," Report No. NASA-TM-81264 (National Aeronautics and Space Administration, 1981).
- <sup>3</sup>C. P. Ellington, C. van den Berg, A. P. Willmott, and A. L. R. Thomas, "Leading-edge vortices in insect flight," *Nature* **384**, 626–630 (1996).
- <sup>4</sup>D. Lintink, W. B. Dickson, J. L. Van Leeuwen, and M. H. Dickinson, "Leading-edge vortices elevate lift of autorotating plant seeds," *Science* **324**, 1438–1440 (2009).
- <sup>5</sup>R. G. Bottom II, I. Borazjani, E. L. Blevins, and G. V. Lauder, "Hydrodynamics of swimming in stingrays: Numerical simulations and the role of the leading-edge vortex," *J. Fluid Mech.* **788**, 407–443 (2016).
- <sup>6</sup>L. W. Carr, "Progress in analysis and prediction of dynamic stall," *J. Aircr.* **25**, 6–17 (1988).
- <sup>7</sup>T. C. Corke and F. O. Thomas, "Dynamic stall in pitching airfoils: Aerodynamics damping and compressibility effects," *Annu. Rev. Fluid Mech.* **47**, 479–505 (2015).
- <sup>8</sup>A.-J. Buchner, J. Soria, D. Honnery, and A. J. Smits, "Dynamic stall in vertical axis wind turbines: Scaling and topological considerations," *J. Fluid Mech.* **841**, 746–766 (2018).
- <sup>9</sup>J. Young, J. C. S. Lai, and M. F. Platzer, "A review of progress and challenges in flapping foil power generation," *Prog. Aerosp. Sci.* **67**, 2–28 (2014).
- <sup>10</sup>T. Kinsey and G. Dumas, "Parametric study of an oscillating airfoil in a power-extraction regime," *AIAA J.* **46**, 1318–1330 (2008).
- <sup>11</sup>W. Geissler, "Flapping wing energy harvesting: aerodynamic aspects," *CEAS Aeronautical Journal* **11**, 379–389 (2020).
- <sup>12</sup>Z. Xiong and X. Liu, "Numerical investigation on evolutionary characteristics of the leading-edge vortex induced by flapping caudal fin," *Phys. Fluids* **31**, 125117 (2019).
- <sup>13</sup>J. Sinha, K. B. Lua, and S. M. Dash, "Influence of the pivot location on the thrust and propulsive efficiency performance of a two-dimensional flapping elliptic airfoil in a forward flight," *Phys. Fluids* **33**, 081912 (2021).
- <sup>14</sup>Y. S. Baik, L. P. Bernal, K. Granlund, and M. V. Ol, "Unsteady force generation and vortex dynamics of pitching and plunging aerofoils," *J. Fluid Mech.* **709**, 37–68 (2012).
- <sup>15</sup>K. K. Chen, T. Colonius, and K. Taira, "The leading-edge vortex and quasisteady vortex shedding on an accelerating plate," *Phys. Fluids* **22**, 033601 (2010).
- <sup>16</sup>X. Zhang and J. U. Schlüter, "Numerical study of the influence of the Reynolds-number on the lift created by a leading edge vortex," *Phys. Fluids* **24**, 065102 (2012).
- <sup>17</sup>X. Li, L.-H. Feng, and Z.-Y. Li, "Flow mechanism for the effect of pivot point on the aerodynamic characteristics of a pitching airfoil and its manipulation," *Phys. Fluids* **31**, 087108 (2019).
- <sup>18</sup>D. Wang, Q. Lin, C. Zhou, and J. Wu, "Aerodynamic performance of a self-propelled airfoil with a non-zero angle of attack," *Phys. Fluids* **34**, 031901 (2022).
- <sup>19</sup>I. Andreu-Angulo, H. Babinsky, H. Biler, G. Sedky, and A. R. Jones, "Effect of transverse gust velocity profiles," *AIAA J.* **58**, 5123–5133 (2020).
- <sup>20</sup>A. R. Jones, "Gust encounters of rigid wings: Taming the parameter space," *Phys. Rev. Fluids* **5**, 110513 (2020).
- <sup>21</sup>A. R. Jones, O. Cetiner, and M. J. Smith, "Physics and modeling of large flow disturbances: Discrete gust encounters for modern air vehicles," *Annu. Rev. Fluid Mech.* **54**, 469 (2022).

<sup>22</sup>J. M. Leung, J. G. Wong, G. D. Weymouth, and D. E. Rival, "Modeling transverse gusts using pitching, plunging, and surging airfoil motions," *AIAA J.* **56**, 3271–3278 (2018).

<sup>23</sup>G. Z. McGowan, K. Granlund, M. V. Ol, A. Gopalarathnam, and J. R. Edwards, "Investigations of lift-based pitch-plunge equivalence for airfoils at low Reynolds numbers," *AIAA J.* **49**, 1511–1524 (2011).

<sup>24</sup>K. H. Elfering and K. O. Granlund, "Lift equivalence and cancellation for airfoil surge–pitch–plunge oscillations," *AIAA J.* **58**, 4629–4643 (2020).

<sup>25</sup>X. Xu and F. D. Lagor, "Quasi-steady effective angle of attack and its use in lift-equivalent motion design," *AIAA J.* **59**, 2613–2626 (2021).

<sup>26</sup>N. J. Wei, J. Kissing, and C. Tropea, "Generation of periodic gusts with a pitching and plunging airfoil," *Exp. Fluids* **60**, 166 (2019).

<sup>27</sup>D. Rival, T. Prangemeier, and C. Tropea, "The influence of airfoil kinematics on the formation of leading-edge vortices in bio-inspired flight," *Exp. Fluids* **46**, 823–833 (2009).

<sup>28</sup>T. Colonius and D. R. Williams, "Control of vortex shedding on two- and three-dimensional aerofoils," *Philos. Trans. R. Soc. A* **369**, 1525–1539 (2011).

<sup>29</sup>N. H. Werner, J. Wang, H. Dong, A. E. Panah, and B. Cheng, "Scaling the vorticity dynamics in the leading-edge vortices of revolving wings with two directional length scales," *Phys. Fluids* **32**, 121903 (2020).

<sup>30</sup>S. Verma, B. R. S. Freeman, and A. Hemmati, "Effects of Reynolds number and average angle of attack on the laminar scaling of oscillating foils," *Phys. Fluids* **34**, 031905 (2022).

<sup>31</sup>M. Zhao, L. Xu, Z. Tang, X. Zhang, B. Zhao, Z. Liu, and Z. Wei, "Onset of dynamic stall of tubercled wings," *Phys. Fluids* **33**, 081909 (2021).

<sup>32</sup>L.-H. Feng, Z.-Y. Li, and Y.-L. Chen, "Lift enhancement strategy and mechanism for a plunging airfoil based on vortex control," *Phys. Fluids* **32**, 087116 (2020).

<sup>33</sup>L. Wang, L.-H. Feng, Y. Liang, Y.-L. Chen, and Z.-Y. Li, "Vortex control strategy for unsteady aerodynamic optimization of a plunging airfoil at a low Reynolds number," *Phys. Fluids* **33**, 117110 (2021).

<sup>34</sup>H. Yu and J. Zheng, "Numerical investigation of control of dynamic stall over a NACA0015 airfoil using dielectric barrier discharge plasma actuators," *Phys. Fluids* **32**, 035103 (2020).

<sup>35</sup>L. Xia, Y. Hua, and J. G. Zheng, "Numerical investigation of flow separation control over an airfoil using fluidic oscillator," *Phys. Fluids* **33**, 065107 (2021).

<sup>36</sup>H. Bao, B. Song, W. Yang, and D. Xue, "The function of the alula with different geometric parameters on the flapping wing," *Phys. Fluids* **33**, 101907 (2021).

<sup>37</sup>K. Ramesh, A. Gopalarathnam, K. Granlund, M. V. Ol, and J. R. Edwards, "Discrete-vortex method with novel shedding criterion for unsteady aerofoil flows with intermittent leading-edge vortex shedding," *J. Fluid Mech.* **751**, 500–538 (2014).

<sup>38</sup>S. Narsipur, P. Hosangadi, A. Gopalarathnam, and J. R. Edwards, "Variation of leading-edge suction during stall for unsteady aerofoil motions," *J. Fluid Mech.* **900**, A25 (2020).

<sup>39</sup>B. L. O. Ramos, W. R. Wolf, C.-A. Yeh, and K. Taira, "Active flow control for drag reduction of a plunging airfoil under deep dynamic stall," *Phys. Rev. Fluids* **4**, 074603 (2019).

<sup>40</sup>M. R. Visbal and D. J. Garmann, "Analysis of dynamic stall on a pitching airfoil using high-fidelity large-eddy simulations," *AIAA J.* **56**, 46–63 (2018).

<sup>41</sup>M. E. Rostami, M. Omidyeganeh, and A. Pinelli, "Direct numerical simulation of the flow around an aerofoil in ramp-up motion," *Phys. Fluids* **28**, 025106 (2016).

<sup>42</sup>Z.-Y. Li, L.-H. Feng, J. Kissing, C. Tropea, and J.-J. Wang, "Experimental investigation on the leading-edge vortex formation and detachment mechanism of a pitching and plunging plate," *J. Fluid Mech.* **901**, A17 (2020).

<sup>43</sup>J. Deparday and K. Mullenens, "Modeling the interplay between the shear layer and leading edge suction during dynamic stall," *Phys. Fluids* **31**, 107104 (2019).

<sup>44</sup>A. Suresh Babu, A. Medina, M. Rockwood, M. Bryant, and A. Gopalarathnam, "Theoretical and experimental investigation of an unsteady airfoil in the presence of external flow disturbances," *J. Fluid Mech.* **921**, A21 (2021).

<sup>45</sup>J. Kissing, J. Kriegseis, Z. Li, L. Feng, J. Hussong, and C. Tropea, "Insights into leading edge vortex formation and detachment on a pitching and plunging flat plate," *Exp. Fluids* **61**, 208 (2020).

<sup>46</sup>A. Widmann and C. Tropea, "Parameters influencing vortex growth and detachment on unsteady aerodynamic profiles," *J. Fluid Mech.* **773**, 432–459 (2015).

<sup>47</sup>K. Onoue and K. S. Breuer, "Vortex formation and shedding from a cyber-physical pitching plate," *J. Fluid Mech.* **793**, 229–247 (2016).

<sup>48</sup>P. J. Ansell and K. Mullenens, "Multiscale vortex characteristics of dynamic stall from empirical mode decomposition," *AIAA J.* **58**, 600–617 (2020).

<sup>49</sup>R. Dunne, P. J. Schmid, and B. J. McKeon, "Analysis of flow timescales on a periodically pitching/surging airfoil," *AIAA J.* **54**, 3421–3433 (2016).

<sup>50</sup>J. O. Dabiri, "Optimal vortex formation as a unifying principle in biological propulsion," *Annu. Rev. Fluid Mech.* **41**, 17–33 (2009).

<sup>51</sup>J. G. Leishman and T. S. Beddoes, "A semi-empirical model for dynamic stall," *J. Am. Helicopter Soc.* **34**, 3–17 (1989).

<sup>52</sup>T. Theodorsen, "General theory of aerodynamic instability and the mechanism of flutter," Report No. NACA-TR-496 (National Advisory Committee for Aeronautics, 1935).

<sup>53</sup>C. Wang and J. D. Eldredge, "Low-order phenomenological modeling of leading-edge vortex formation," *Theor. Comput. Fluid Dyn.* **27**, 577–598 (2013).

<sup>54</sup>X. Xia and K. Mohseni, "Lift evaluation of a two-dimensional pitching flat plate," *Phys. Fluids* **25**, 091901 (2013).

<sup>55</sup>R. Fernandez-Feria and J. Alaminos-Quesada, "Unsteady thrust, lift and moment of a two-dimensional flapping thin airfoil in the presence of leading-edge vortices: A first approximation from linear potential theory," *J. Fluid Mech.* **851**, 344–373 (2018).

<sup>56</sup>S. Otomo, S. Henne, K. Mullenens, K. Ramesh, and I. M. Viola, "Unsteady lift on a high-amplitude pitching aerofoil," *Exp. Fluids* **62**, 6 (2021).

<sup>57</sup>K. Kamrani Fard, V. Ngo, and J. A. Liburdy, "A leading-edge vortex initiation criteria for large amplitude foil oscillations using a discrete vortex model," *Phys. Fluids* **33**, 115123 (2021).

<sup>58</sup>Y. Hirato, M. Shen, A. Gopalarathnam, and J. R. Edwards, "Flow criticality governs leading-edge-vortex initiation on finite wings in unsteady flow," *J. Fluid Mech.* **910**, A1 (2021).

<sup>59</sup>A. Saini, S. Narsipur, and A. Gopalarathnam, "Leading-edge flow sensing for detection of vortex shedding from airfoils in unsteady flows," *Phys. Fluids* **33**, 087105 (2021).

<sup>60</sup>T. M. Faure and C. Leogrande, "High angle-of-attack aerodynamics of a straight wing with finite span using a discrete vortex method," *Phys. Fluids* **32**, 104109 (2020).

<sup>61</sup>J. Li and Z.-N. Wu, "A vortex force study for a flat plate at high angle of attack," *J. Fluid Mech.* **801**, 222–249 (2016).

<sup>62</sup>J. Li, Y. Wang, M. Graham, and X. Zhao, "Vortex moment map for unsteady incompressible viscous flows," *J. Fluid Mech.* **891**, A13 (2020).

<sup>63</sup>K. Menon and R. Mittal, "Quantitative analysis of the kinematics and induced aerodynamic loading of individual vortices in vortex-dominated flows: A computation and data-driven approach," *J. Comput. Phys.* **443**, 110515 (2021).

<sup>64</sup>G. H. Vatistas, V. Kozel, and W. C. Mih, "A simpler model for concentrated vortices," *Exp. Fluids* **11**, 73–76 (1991).

<sup>65</sup>S. Narsipur, A. Gopalarathnam, and J. R. Edwards, "Low-order model for prediction of trailing-edge separation in unsteady flow," *AIAA J.* **57**, 191–207 (2019).

<sup>66</sup>A. Suresh Babu, K. Ramesh, and A. Gopalarathnam, "Model reduction in discrete-vortex methods for unsteady airfoil flows," *AIAA J.* **57**, 1409–1422 (2019).